LUNDS UNIVERSITET

Simulating Quantum Cascade Lasers with the Position and Energy Resolving Lindblad approach

Maitane Muñoz Basagoiti

Thesis submitted for the degree of Master of Science
Project duration: 9 months, 60 hp

Supervised by Andreas Wacker

Department of Physics
Division of Mathematical Physics
May 2019

Abstract

Over the past two decades, Quantum Cascade Lasers (QCLs) have become an increasingly popular source for mid-infrared and terahertz radiation. Nowadays, their experimental development progresses fast with the aid of computer simulations. These reproduce carrier dynamics in the gain medium of the laser based on different transport models. A fast and reliable simulation package for QCLs is key for the future realization of optimized structures. In this thesis, we have tested the validity of a recently presented QCL simulation package called Lindblad-QCL. The package is based on a heuristic and phenomenological density matrix approach: the Position and Energy Resolving Lindblad approach. We have run several QCL simulations using the Lindblad-QCL simulation package and compared the results to experimental data. These simulations provide a good qualitative description of the QCL active medium. We have extended the simulation package implementing interface roughness scattering and analysed the impact of temperature in the simulations. The results we present in this thesis show that Lindblad-QCL is a candidate to become a strong QCL simulation package.

Abbreviations

CB ..... Conduction Band

EMC ..... Ensemble Monte-Carlo

IFR ..... Interface Roughness

IR ..... InfraRed

LASER ..... Light Amplification Through Stimulated Emission of Radiation

LASIK ..... Laser Assisted in Situ Keratomileusis

LGKS ..... Lindblad-Gorini-Kossakowski-Sudarshan

LLS ..... Lower Laser State

LO ..... Longitudinal Optical

LQCL ..... Lindblad-Quantum Cascade Laser

MBE ..... Molecular Beam Epitaxy

MOQVD ..... Metal-Organic Chemical Vapor Deposition

NDR ..... Negative Differential Resistivity

NEGFs ..... Non-Equilibrium Green's Functions

PDR ..... Positive Differential Resisitivity

PERLind ..... Position and Energy Resolving LINDblad

QCL ..... Quantum Cascade Laser

THz ..... TeraHertz

ULS ..... Upper Laser State

UV ..... UltraViolet

VB ..... Valence Band

WS ..... Wannier-Stark

Acknowledgements

I would like to thank my supervisor Andreas Wacker for his support and dedication throughout this thesis, for always having his door open and taking the time to help me understand this project. Thank you! I would also like to thank the Non-Equilibrium Quantum Transport in Nanosystems group for making the experience enjoyable and inspiring. I thank Gediminas Kiršanskas for helping me decode his code and for taking the time to answer my e-mails, and Martin Franckié, for a very valuable discussion on scattering mechanisms and introducing me to Aftershoq.

I would like to apologise to my office-mates, with whom I have shared a crowded and noisy room for a year, for stealing their CPU cores from time to time for my calculations. Thank you for the friendly atmosphere in our office! I specially thank Philipp Stürmer and Erik Linnér for their suggestions on this report, which have helped improve it, and our insightful discussions - sometimes on Physics, but mostly on life. I cannot imagine Lund without the coffee breaks I have taken with Paul André throughout these two years. For them, I thank him.

Finally, I thank my family for their encouragement and patience, even from afar.

Aiteterentzat
To my grandfather

Contents

Chapter 1 | Introduction

The celebration of the International Year of Light in 2015 commemorated the great impact of photonics and light-based technologies on human progress [1]. From radiowaves and sunlight to X-rays and γ-rays, we are surrounded by photonic sources of different energies spread all over the electromagnetic spectrum. These can be found in fields like medicine, telecommunications and industry [2]. Among the many achievements in photonics, the LASER (Light Amplification through Stimulated Emission of Radiation) is perhaps the best example of the power of light. Lasers are characterized by a narrow linewidth and the emission of coherent radiation. Such unique properties make them suitable for high precision medical procedures (e.g. LASIK[1] procedure for eye surgery), sensitive optical sensors and fiber optical communication [2]. The laser spectrum spans from the Ultraviolet (UV) (10 -400 nm) to the Infrared (IR) (40-100 THz and 1-8 μm [3, 4]) and even more importantly, Terahertz (THz) frequencies (0.3-10 THz and 30 μm to 1 mm [3]) [5].

The experimental realization of the first operating Quantum Cascade Laser (QCL) by Faist *et al.* in 1994 [6], inspired by the work of Esaki and Tsu on superlattices [7], opened a new research path in the field of laser technology. The QCL spectrum ranges from the mid-IR region to the challenging THz frequency band and it currently extends from 2.6 μm to 400 μm (with the aid of a magnetic field) [8, 9, 10]. Nowadays, QCLs have become the main source of IR radiation, vastly employed in chemical spectroscopy and applications such as gas monitoring [10, 11, 12]. Moreover, QCLs are good candidates to bridge the so-called *THz-gap* of uncovered frequencies between electronics and optics [13] after the development of the first operating THz-QCL in 2002 [14]. Frequencies in the THz band are useful for biological spectroscopy, imaging of molecules and astronomy; atmospheric spectroscopy for environmental monitoring or protein dynamics, for instance, exhibit absorption peaks at THz frequencies [5]. Furthermore, QCLs comprise all the benefits of a semiconductor laser in terms of compactness, efficiency and reduced manufacture costs, which makes them attractive THz and IR radiation sources [3, 10].

Although much progress has been achieved in the past two decades for output power and high operating temperature for mid-IR QCLs [15], QCL technology is still in development. The quest for room temperature THz-QCLs continues [16]. Operation temperatures of 230 K, at which it would be possible to cool the device electronically (*Peltier cooling*), have not been published yet for THz-QCLs [10]. Current lines of research focus on reaching higher temperatures for THz-QCLs and increasing wall-plug efficiency for all devices (currently at 20-27% for mid-IR QCLs at room temperature [3, 10]). All this work converges towards a common goal: the industrial manufacturing and generalized use of QCLs in electronics in the future.

[1] *Laser assisted in Situ Keratomileusis* (LASIK) is a medical procedure used to correct the cornea in patients with myiopia, astigmatism or hyperopia.

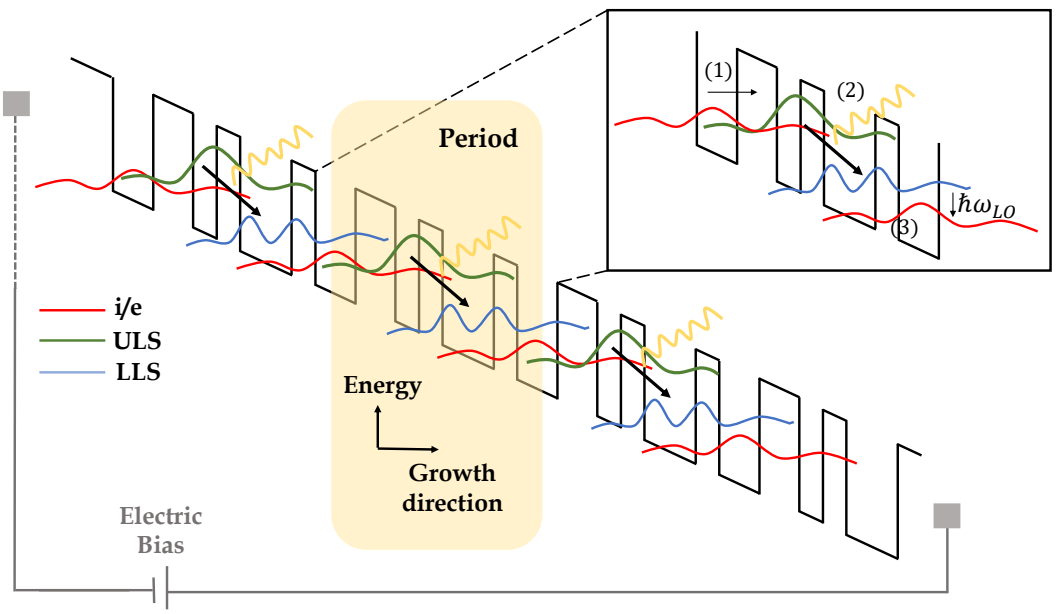

Figure 1.1: Diagram showing the basic principle of a QCL. The tilted conduction band edge and quantized well states (injector (i), extractor (e) and upper (ULS) and lower (LLS) laser states) are shown with solid lines. Inset: Example of a basic period design from [17]: (1) Carriers tunnel from i to ULS. (2) A photon is emitted in the ULS to LLS transition. (3) Phonon extraction mechanism from ULS to e, where $\hbar\omega_{LO}$ is the energy of a Longitudinal-Optical (LO) phonon. The idea for the diagram was inspired by Fig. 1.8 in [18].

1.1 Introduction to Quantum Cascade Lasers

QCLs constitute a unique type of semiconductor laser. Their optical medium consists of a semiconductor heterostructure that produces gain when biased along the growth direction (z-direction), as first postulated by Kazarinov and Suris in 1971 [19]. In conventional lasers, stimulated emission takes place between the natural electronic levels of the atoms in the gain material. This occurs when the number of electrons in the Upper Laser State (ULS) is larger than the number of electrons in the Lower Laser State (LLS), so-called *population inversion*. Unlike regular atomic lasers, QCLs rely on population inversion between artificially engineered energy levels. These arise in the Conduction Band (CB) as a result of the underlying layered structure of the device [10]: the alternating stacking of semiconductor materials (that is, a heterostructure) with different band gaps yields a CB edge of sequenced quantum wells along the growth direction (see Fig. 1.1). The CB offset between the materials delimits a well and acts as a barrier, trapping electrons in quantized energy levels. In the transverse direction (xy-plane), assumed to be infinite, electrons have no constraints and move as free particles [3, 12]. An electronic state is then the combination of the quantized well levels and the transverse free particle wavefunction.

In a QCL, photons are emitted at *intersubband* transitions, i.e. between the quantized levels in the one-dimensional (1D) multiple quantum well structure. In regular semiconductor lasers, photons are emitted after the radiative recombination of an electron-hole pair across the band gap [10]. In contrast, QCL emission solely depends on electronic jumps within the CB. This is why QCLs are also known as *monopolar* semiconductor lasers [10]. Thus, the lasing frequency in a QCL is not constrained by the band gap of

the material, but by the energy difference between the energy levels in the CB [10, 12]. Emission in the THz and mid-IR range becomes possible with heterostructures based on III-V type semiconductors such as GaAs, InP and alloys like $Al_xGa_{1-x}As$ and $In_yGa_{1-y}As$, where x and y indicate the alloy fraction [12]. The *period* or *module* of a QCL contains a finite series of barriers and wells, and it is designed to host a radiative transition (see Fig. 1.1, inset). This module is the basic unit necessary for the emission of a photon in a QCL. Its periodic repetition along the growth direction results in optical gain, that is, multiple photoemissions. Laser operation is achieved when optical gain overcomes mirror, cavity and waveguide losses.

Population inversion in a QCL is driven by an external electric field, which pumps the electrons into the CB ladder. The electric field forces carriers to *cascade* down the structure. Electrons are then recycled in each period for a new radiative transition. A single cascading electron can potentially yield as many photons as periods in the gain medium [12]. The applied bias, assumed to drop homogeneously along the heterostructure in this thesis, tilts the CB edge and modifies the spacing between the energy levels in the wells (see Fig. 1.1). As the bias increases, the levels displace in energy and align with other levels in neighbouring periods. The alignment of the well levels leads to resonant tunnelling through the barriers [19] or favours scattering mechanisms like Longitudinal Optical (LO) phonon scattering. The design of the QCL module exploits these phenomena to efficiently inject electrons into the ULS and quickly depopulate the LLS. Transport of carriers in the structure is also assisted or degraded by other scattering mechanisms such a impurities, Interface Roughness (IFR) or electron-electron interactions [12].

The heterostructure growth process enables full control of gain medium design. Consequently, it allows the engineering of the quantized well levels [10, 12]. Design strategies differ for THz and IR-QCLs due to the energy ranges involved. For instance, in GaAs, the energy of a LO phonon ($\sim$36 meV) is larger than the level spacing in THz-QCLs and smaller than that of IR-QCLs, motivating different extraction and injection mechanism designs for the basic module [4, 20, 21]. See the inset in Fig. 1.1 for an example of a design with tunneling injection and phonon extraction. These mechanisms are tailored to provide the desired energy transition and corresponding emission frequency. For a comprehensive review on THz-QCL gain medium designs, the reader is referred to [4]; a review of the current state of IR-QCL designs can be found in [20].

1.2 Motivation of the thesis

QCLs are exemplary devices to study the microscopic phenomena of the solid state world. A full comprehension of the device requires the use of Quantum Mechanics, Solid State Theory and Material Science, as well as state-of-art experimental techniques like Molecular Beam Epitaxy (MBE) or Metal-Organic Chemical Vapor Deposition (MOCVD). Aside from improving our models and understanding of the nanoscale, QCL simulations serve as probes for optimized active region designs. The information extracted from simulations can be used to improve the experimental performance of the devices [10]. Examples of optimized structures derived from theoretical simulations can be found in [16, 22, 23].

A laser is a system out of equilibrium, where a detailed modeling of carrier dynamics is key for an accurate simulation of the device. There exists a widely varied range

of approaches to simulate carrier transport in QCLs: from semiclassical rate equations and phenomenological approaches, to quantum-mechanical methods that are entirely self-consistent [10, 24, 25]. Far from trivial, the underlying physics of non-equilibrium quantum transport in QCLs poses a challenge: describing an *open* quantum system - the electrons in the CB - in contact with its *environment* - the lattice, which acts as a reservoir. The main complexity of this problem lays in accounting for the environment's infinite degrees of freedom, which makes it impossible to exactly describe the evolution of the system.

The Position and Energy Resolving Lindblad (PERLind) approach is a recently presented phenomenological and heuristic density matrix method. It models quantum transport in non-equilibrium quantum systems coupled to their environment [26]. Hence, it can be used to simulate carrier dynamics in QCLs. PERLind's foundations lay on the system-environment coupling agents, responsible for the electron transitions. These agents are modelled as jump operators that contain information about the location and energy of the transitions driving transport in the system. The PERLind approach for the simulation of quantum transport in QCLs is implemented through the Lindblad-QCL (LQCL) Python package [26]. The simulation package models the QCL heterostructure and provides relevant laser observables such as current density, occupation probability of the laser states and gain spectrum. PERLind's major asset is its light computation load in comparison to other existing QCL simulation approaches like the computationally heavier Non-Equilibrium Green's Functions (NEGF) [25]. PERLind allows for fast time-resolved calculations to compute laser gain. Therefore, it is important to establish a relation between the scope of the PERLind approach and the reliability of LQCL as a fast and efficient QCL simulation package.

LQCL has not been thoroughly tested before for many different QCLs [26]. Thus, the purpose of this thesis is to check the validity and functionality of the LQCL computational package. This is done by simulating an ensemble of QCLs and comparing the theoretical predictions with experimental results. Here, the focus is set in simulating THz-QCLs because of the unsolved questions that revolve around their operation. A few IR-QCLs are also simulated to test the extension of LQCL's validity. Our preliminary simulations highlight LQCL's general underestimation of the current density, possibly signalling neglected scattering mechanisms in the code. An accurate description of the subband electronic temperature also proves to be relevant to improve the performance of the package. Motivated by these findings, the thesis aims to further complete the LQCL computational package by studying the impact of assuming thermal subband distributions in the CB. In addition, IFR scattering is implemented in the package to quantitatively improve the simulations. LQCL is also compared to the well-established NEGFs code used by our group [25].

This work is organised as follows: Chapter 2 introduces the reader to the scattering mechanisms that drive transport in the heterostructure, as well as the techniques to model the QCL active region and transport approaches. Chapter 3 presents a density matrix theory for non-equilibrium quantum transport together with the PERLind approach. Here, the LQCL package is introduced. In Chapter 4 we present the results obtained with the LQCL package and compare them to experimental data. These results are discussed and improvements are attempted. In Chapter 5, the numerics of the LQCL code are given. Finally, Chapter 6 gathers the conclusions and proposes an outlook from this project.

Chapter 2 | QCL Fundamentals: Modelling the device

The foundations of accurate QCL simulations rely on understanding the microscopic phenomena that govern carrier transport at the nanoscale. For that purpose, this chapter is divided in two main sections. Section 2.1 serves as an introduction to the main scattering mechanisms that drive carrier dynamics in a QCL. Section 2.2 is devoted to QCL modeling. Here, the tools necessary to simulate the device are provided and the approaches to describe carrier transport in QCLs briefly reviewed. This chapter aims to prepare the reader for Chapter 3, where we will focus on one method for QCL simulation: the PERLind approach.

2.1 Scattering mechanisms in QCLs

Scattering can be *elastic* or *inelastic* (see Fig. 2.1, a). In elastic scattering, energy is conserved $E_f = E_i$, while inelastic scattering mechanisms involve the exchange of energy through e.g. the emission or absorption of photons or phonons. Examples of inelastic scattering mechanisms are LO-phonon scattering, and spontaneous and stimulated emission. In contrast, IFR and ionic impurities are connected to elastic processes. In QCLs, scattering mechanisms yield *intrasubband* and *intersubband* transitions within the CB of the heterostructure (see Fig. 2.1, b). In an intrasubband transition, electrons remain in the same quantized energy level but their momentum changes. During an intersubband transition, electrons jump to a different energy level. However, an intersubband transition can also yield a change in momentum if it is not purely vertical in momentum.

In QCLs, transport is not predominantly driven by radiative transitions, i.e. spontaneous and stimulated emission, as it is in regular lasers. Instead, scattering mechanisms such as LO-phonon scattering, impurity and IFR scattering or carrier-carrier interactions dominate the carrier dynamics. Stimulated emission can also become a dominating contributor to transport in the device as it is enhanced by the lasing optical field [27]. These mechanisms perturb electrons out of their heterostructure eigenstates and are vital to understand non-equilibrium carrier dynamics [28]. The thickness of the heterostructure barriers, doping density or intersubband spacing of the QCL, among others, enhance or suppress the above scattering phenomena. The relevance of a scattering mechanism is given by the scattering time associated to it. The shorter this time, the more frequent the process is. Transport is dominated by the mechanism that exhibits the shortest scattering time (or alternatively, the largest scattering *rate*) over the rest of the phenomena. Times can vary from a few picoseconds to nanoseconds and depend on the design of the QCL [10, 12]. In Ref. [29], Ferreira and Bastard discuss scattering times for single quantum well structures, which can be taken as a first estimation for scattering times in QCLs.

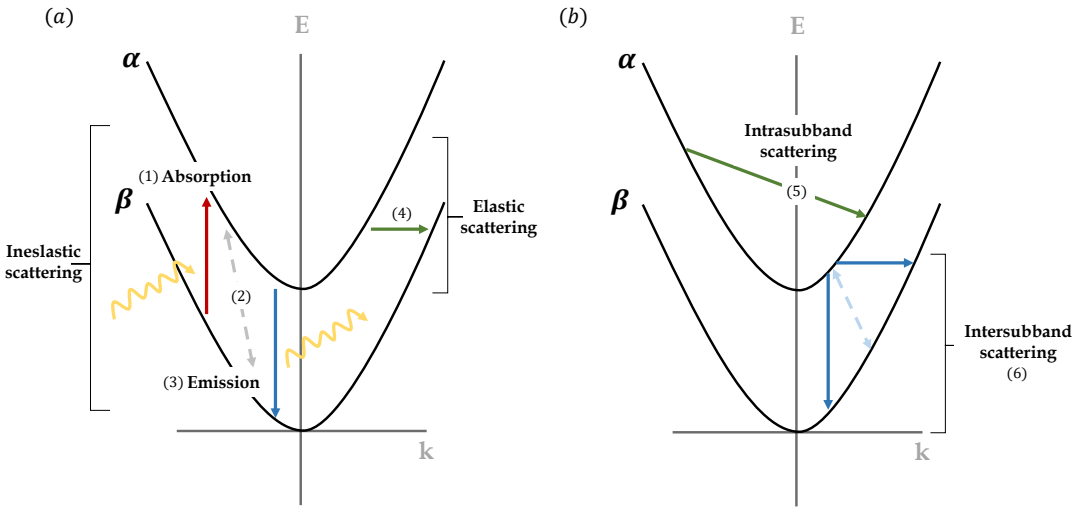

Figure 2.1: Diagram of electronic subbands. (a) The elastic and inelastic scattering mechanisms. The subbands are labelled as α and β. (1, 3) Vertical absorption and emission mechanisms. (2) Diagonal scattering transition. (4) Elastic scattering. (b) Intrasubband (5) and intersubband (6) transitions.

2.1.1 Phonon scattering

Atoms in a lattice oscillate collectively around their equilibrium positions (i.e. lattice points) with frequency $\omega(\boldsymbol{q})$ and amplitude $\boldsymbol{\varepsilon}$. From a classical viewpoint, a collective oscillation of the lattice atoms at a single, well-defined frequency constitutes a *normal mode*, i.e. a solution of the displacement field of the lattice. From the quantum viewpoint, a phonon is an elementary unit of vibration of the this field. These quanta are classified into *optical* and *acoustic* phonons, depending on the motion of two adjacent atoms. An acoustic phonon is formed by atoms displa-cing in the same direction as the propagation of the wave, while for an optical phonon adjacent atoms vibrate in opposite directions. When the propagation of the vibration wave $\boldsymbol{\varepsilon}$ and its wavevector $\boldsymbol{q}$ are parallel, $\boldsymbol{\varepsilon} \parallel \boldsymbol{q}$, the phonon is called *longitudinal*, while a propagation perpendicular to the wavevector, $\boldsymbol{\varepsilon} \perp \boldsymbol{q}$, defines *transverse* phonons [10, 30].

In our semiconductor heterostructure, the energy exchange between charged carriers and the lattice results in inter- and intrasubband electronic transitions where optical phonons are absorbed and/or emitted. In fact, many QCL active region designs exploit them as a depopulation and injection mechanism of the laser levels (see Fig. 1.1, inset); such is the case for resonant-injection and extraction designs in [16, 17]. Furthermore, optical phonons thermalize carriers into the QCL subbands by helping them lose kinetic energy [31]. However, optical phonons are also responsible for phenomena that degrade laser operation. An example of that is *thermal backfilling*, where the emptied LLS is filled again through the absorption of phonons. This thermally activated phenomenon reduces population inversion and consequently, optical gain [4].

The electron-phonon interaction is described by the Fröhlich Hamiltonian [30],

$$\hat{H}_{\text{el-ph}} = \sum_{\boldsymbol{k},\boldsymbol{q},q_z} \sum_{\alpha,\beta} M^{q_z}_{\beta\alpha}\, \mathrm{g}_{\boldsymbol{q},q_z}\, \hat{c}^{\dagger}_{\beta,\boldsymbol{k}+\boldsymbol{q}}\, \hat{c}_{\alpha,\boldsymbol{k}}\, \hat{b}_{\boldsymbol{q},q_z} + H.c.. \tag{2.1}$$

Here, *H.c.* stands for Hermitian conjugate, $\boldsymbol{k}$ is the crystal momentum of the electrons and $\boldsymbol{q} = (q_x, q_y)$ and q_z are the lateral and longitudinal components of the phonon momentum, respectively; $\mathrm{g}_{\boldsymbol{q},q_z}$ is a function accounting for the coupling strength, $\hat{c}_{\boldsymbol{q},q_z}(\hat{b}_{\boldsymbol{q},q_z})$ is the fermionic (bosonic) annihilation operator, $\hat{c}^{\dagger}_{\boldsymbol{q},q_z}(\hat{b}^{\dagger}_{\boldsymbol{q},q_z})$ is the fermionic (bosonic) creation operator and $M^{q_z}_{\beta\alpha}$ is the overlap integral of the electronic states α and β [26],

$$M^{q_z}_{\beta\alpha} = \int \mathrm{d}z\ \psi^{\star}_{\beta}(z) e^{iq_z z} \psi_{\alpha}(z). \tag{2.2}$$

Each phonon couples to charge carriers differently. Therefore, the coupling strength function, $\mathrm{g}_{\boldsymbol{q},q_z}$, depends on the phonon type. In the case of quantum transport in QCLs, the most relevant phonons are polar LO-phonons. Their relevance stems from the growth materials used for QCLs, polar III-V semiconductors, which have two different atoms with effective charges in the unit cell, e.g. GaAs [10]. The vibration of these two atoms in opposite directions (that is, an optical phonon) yields a net charge displacement. As a result, a local dipole moment forms within the unit cell. The collective oscillation of this optical mode constitutes an oscillating macroscopic polarization, which strongly couples to the electrons in the structure. Only longitudinal phonons contribute to the interaction, as $\hat{H}_{\text{el-ph}} \propto \boldsymbol{\varepsilon} \cdot \boldsymbol{q}$ (see [30], Chapter 4, for a detailed construction of the hamiltonian). LO-phonons can be assumed to have a constant energy $\hbar\omega_{LO}$, disregarding dispersion ($\omega(\boldsymbol{q}) \approx \omega$). The LO-phonon polar coupling function is given by [26, 30]

$$\mathrm{g}_{\boldsymbol{q},q_z} = \frac{i}{\sqrt{AL}} \sqrt{\frac{e^2\hbar\omega_{LO}}{2\epsilon_0\epsilon_p}} \frac{1}{\sqrt{\boldsymbol{q}^2 + q_z^2}}, \tag{2.3}$$

where L is a normalization length and A is the lateral area of the QCL. In the expression above, ϵ_0 is vacuum permittivity and $\epsilon_p^{-1} = \epsilon_{\infty}^{-1} - (\epsilon^{(0)})^{-1}$ where ϵ_{∞} and $\epsilon^{(0)}$ are the dielectric constants above and below the LO-phonon energy, respectively [26]. ϵ_p quantifies the polarization of the material without the contribution from the ions in the lattice. A detailed derivation of equation (2.3) can be found in [30].

When the intersubband spacing matches $\hbar\omega_{LO}$, the emission or absorption of an LO-phonon is highly favoured, a phenomenon known as *resonance*. In that case, the intersubband transition is essentially vertical in momentum space (see Fig. 2.1) with a very short scattering time (0.5-1 ps) [11, 32]. Under such subband alignment conditions, LO-phonon scattering becomes the dominant mechanism in the device. For acoustic phonons, the scattering rates are significantly larger, from 80 ps to 240 ps [12]. Their impact on carrier transport is very small in comparison to that of LO-phonons. Therefore, acoustic phonons can be safely neglected in transport simulations of QCLs.

2.1.2 Impurity scattering

The semiconductor heterostructure of a QCL is fed with carriers through *donor* atoms. When a lattice atom is substituted by a donor, the latter can supply the outermost valence electrons for laser operation. Typically, QCLs are doped with Silicon, which occupies Gallium sites and acts as a n-type donor. However, the placement of such donor breaks the periodicity of the lattice with its associated extra positive charge (see Fig. 2.2) and perturbs the eigenstates of the QCL system. These donor ions constitute the impurities

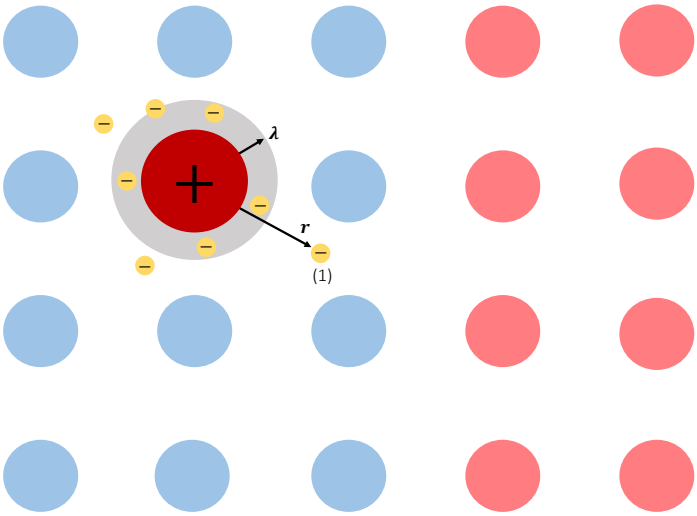

Figure 2.2: Schematic representation of an ionic impurity in the semiconductor heterostructure of a QCL. The donor atom (red spot) is surrounded by a screening cloud (grey region) created by the carriers in the lattice (small yellow spots). The potential that perturbs electron (1) at a distance r from the donor atom is screened by the cloud, with a screening length λ. The blue and pink atoms in the lattice represent two different semiconductor layers in the QCL heterostructure.

of layered heterostructure. Moreover, the mechanism is relevant for quantum transport in QCL devices with high carrier concentration, where the number of impurity scatterers is larger. The number of impurities equals the electronic doping density (typically $\sim 10^{16}$ impurities/cm^3 [16]). The associated scattering times are longer than those for LO-phonon scattering. Ferreira and Bastard [29] show that the scattering times range from 20 to 50 ps for single-quantum wells and 0.1 and 10 ps for multiple quantum wells.

Ionic impurities are an elastic scattering mechanism that is modelled through Coulombic forces. The potential that describes the interaction of an electron with a single ion, with charge Z_i at position z_i is [10, 33]

$$V_i(r) = -\frac{1}{4\pi\epsilon_0\epsilon_r} Z_i e^2 \left(\frac{1}{|\boldsymbol{r} - \boldsymbol{r}_i|^2 + |z - z_i|^2} \right)^{1/2}, \tag{2.4}$$

where e is the electron charge, and ϵ_0 and ϵ_r are the vacuum and relative permittivity, respectively. Nevertheless, the potential created by the i-th impurity will be screened by other charged carriers in the lattice (see Fig. 2.2). The screening *"damps"* the potential in equation (2.4) as [33]

$$\frac{1}{r} \xrightarrow{\text{screening}} \frac{1}{r} e^{-r\lambda}, \tag{2.5}$$

which has now the shape of a Yukawa potential, with λ as the inverse screening length. Screening is a very complex phenomenon. Its accurate modelling constitutes a field of research by itself, and going into details is out of the scope of this thesis. The interested reader is referred to Refs. [10] and [12] (Chapter 5) for reviews on different screening models used in QCL simulations and their impact on the lifetime of the heterostructure eigenstates.

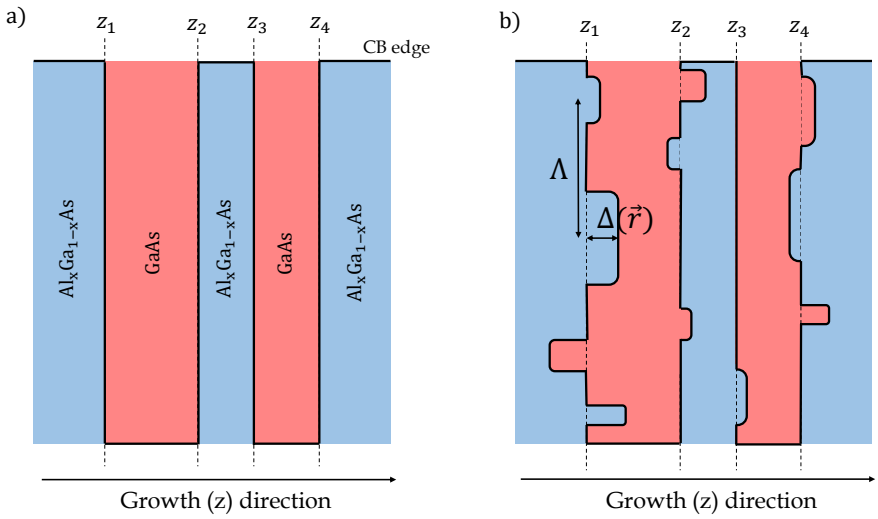

Figure 2.3: (a) Ideally smooth QCL heterostructure. The interfaces are sharp and perfect. (b) Schematic representation of a real QCL heterostructure. Random fluctuations of height $\Delta(\vec{r})$ can be seen at the interfaces in z_i, where i labels the interface. The correlation length between the height fluctuations is measured by Λ.

2.1.3 Interface roughness scattering

The late realization of QCLs, two decades after they were theoretically predicted [6, 19], stems from a lack of experimental tools for their development. Growth techniques like MBE and MOCVD have been fundamental for QCLs. These methods enable the layered growth of III-V semiconductors at the resolution of an atomic layer, producing almost perfectly sharp interfaces for the wells and barriers of the active region of a QCL [12]. However, deviations from the ideally smooth well or barrier width exist (see Fig. 2.3). These deviations perturb the lattice potential, just as ionic impurities or phonons, breaking the translational invariance of the in-plane direction.

IFR scattering is an elastic scattering mechanism that arises from the random barrier width fluctuations at the interfaces of the QCL heterostructure. It is particularly relevant in lasers with short wavelengths ($\lambda \leq 5$ μm) and QCL modules with thin barriers [12]. In general, this mechanism will have a more prominent role in IR-QCLs due to their shorter wavelength. Two main parameters model the fluctuations at the interface: the correlation length between the fluctuations, Λ, and the standard deviation of the barrier width, Δ. Typically, $\Lambda \sim 10$ nm while $\Delta \sim 0.1$-0.4 nm [10, 34]. The correlation function accounting for the barrier width fluctuations at the interface is usually modelled either as a *Gaussian* function [3, 34],

$$\langle \Delta(\boldsymbol{r})\Delta(\boldsymbol{r}+\boldsymbol{d})\rangle = \Delta^2 \exp\left(-\frac{|\boldsymbol{d}|^2}{\Lambda^2}\right) \tag{2.6}$$

or as an *exponential* function [3, 34],

$$\langle \Delta(\boldsymbol{r})\Delta(\boldsymbol{r}+\boldsymbol{d})\rangle = \tilde{\Delta} \exp\left(-\frac{|\boldsymbol{d}|}{\tilde{\Lambda}}\right). \tag{2.7}$$

The parameters Δ, Λ, $\tilde{\Delta}$ and $\tilde{\Lambda}$ define the correlation length and fluctuation height in the Gaussian and exponential models, respectively [3]. The choice of correlation function de-

pends on the type of interface we are interested in modeling [34]. Gaussian functions model smooth height deviations at the interface, while sharp fluctuations are more accurately described with exponential functions. Nevertheless, the exact profile of the interfaces is unknown, which means that the above Δ and Λ must be regarded as fit parameters. A thorough discussion of the impact of IFR scattering in QCL simulations can be found in [10, 35], where the choice of (2.6) and (2.7) is compared.

2.2 Modeling Techniques for QCLs

Now that we have identified the main physical mechanisms that drive carrier transport in QCLs, we can focus on modeling the device. In fact, detailed modeling of the QCL active region is crucial for a realistic simulation. For that purpose, the theoretical description of a QCL is divided in two parts: the computation of eigenstates of the heterostructure and the description of carrier transport. Fundamentally, these two parts are reduced to answering two questions: *What states do carriers occupy?* (sections 2.2.1 and 2.2.2) and *how do carriers move in the heterostructure?* (section 2.2.3).

2.2.1 Heterostructure eigenstates

A common approach to the computation of electronic states in a heterostructure is the use of envelope functions, $\Psi(\boldsymbol{r})$ [36]. In the effective mass approximation, envelope functions are described within the BenDaniel-Duke model, i.e. only the conduction band is considered [37]. Envelope functions satisfy the time-independent Schrödinger equation,

$$\left[-\frac{\hbar^2(\partial_x^2+\partial_y^2)}{2m^{\parallel}(z)}+\partial_z\frac{1}{m_c(z)}\partial_z+V(z)+E_c(z)-E\right]\Psi(\boldsymbol{r})=0, \tag{2.8}$$

where $V(z)$ is the lattice potential, $E_c(z)$ is the CB energy, and m_c and $m^{\parallel}$ are the effective masses in the growth and transverse direction, respectively [10]. The in-plane coordinates (x, y) can be decoupled from the longitudinal direction z by assuming that electrons behave as free particles, i.e. plane waves, in the transverse direction (see Fig. 2.4). This motivates the ansatz

$$\Psi_{n,\boldsymbol{k}}(\boldsymbol{r})=\frac{1}{\sqrt{A}}\psi_n(z)e^{i(k_x x+k_y y)} \tag{2.9}$$

for the envelop function $\Psi(\boldsymbol{r})$, where A is the transverse section of the device [10]. The total energy E of the state is given by the sum of the eigenvalue corresponding to the quantized well level and the kinetic energy of the transverse modes,

$$E=E_n+\frac{\hbar^2|\boldsymbol{k}|^2}{2m_{\parallel}}. \tag{2.10}$$

Band non-parabolicity effects are incorporated through an energy dependent effective mass, which also includes contributions from the Valence Band (VB) [10, 12]. See Chapter 3 in [3] for a complete description of the Two-Band model. Finally, with the ansatz (2.9), the computation of the heterostructure eigenfunctions is reduced from three to a 1D problem: the calculation of $\psi_n(z)$.

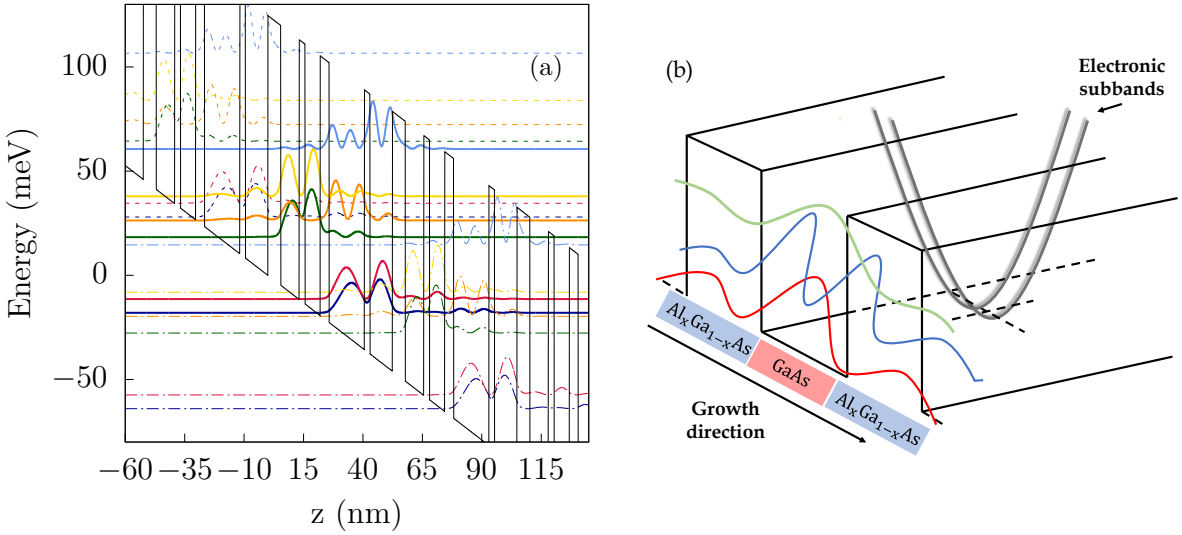

Figure 2.4: (a) First six Wannier-Stark (WS) states of the device in [38]. The active region is a four-well phonon extraction design. The eigenstates of the central period are shown with solid lines. Neighbouring left (right) states are shown in dashed (dotted) lines. (b) Schematic diagram of eigenstates of a GaAs/$Al_xGa_{1-x}As$ heterostructure. Electrons move as free particles in the transverse (x, y) direction, where we see the parabolic dispersion functions. The quantized well states arise in the longitudinal or growth direction, z, as a result of the conduction band offset.

2.2.2 Quantum Wells and the Wannier-Stark Ladder

Most graduate Physics students are familiar with the infinite Quantum Well problem, where bound states arise as a result of the confining potential. An analogous set-up characterizes the quantized $\psi_n(z)$ states at the multi-quantum well structure in QCLs [3]. These states are solution to equation (2.8). They are extended all over the heterostructure, exceeding the semiconductor barriers for large z (see Fig. 2.4, a). As a result, they are characterized by a finite state lifetime. They are referred to as *quasi-bound* or *quasi-stationary* states [10]; that is, they decay over time. However, the relevant laser states are typically deep within the quantum well and can, nonetheless, be considered strongly bound. Moreover, their lifetime is determined by the scattering mechanisms in the structure rather than their intrinsic finite lifetime [10].

There exist several techniques to compute the eigenstates $\psi_n(z)$ of a periodic multiple well structure, see [10, 28] for detailed reviews. In this thesis, the eigenfunctions of the unbiased heterostructure are computed through the application of Bloch's theorem. The theorem exploits the periodicity of the multi-well active region of a QCL [30]. Bloch's functions, $\psi_{\nu\boldsymbol{q}}(z)$, are labelled by the crystal momentum $\boldsymbol{q}$ and subband index ν. They are extended all over the structure and thus, *delocalized*. A linear superposition of Bloch's functions yields a set of *localized* states known as Wannier states, $\Psi_\nu(z)$,

$$\Psi_\nu(z) = \frac{d}{2\pi}\int dq\; e^{i\alpha(q)}\psi_{\nu\boldsymbol{q}}(z) \tag{2.11}$$

where d is the length of a period and the phase $\alpha(q)$ is chosen to maximize the localization of the states [28]. Modeling QCLs requires a localized basis, as it is important to understand the distribution of carriers in the wells of a period. This information is

relevant for transport properties - specially for the approach to transport we will be using, PERLind. Wannier states constitute a finite orthonormal set of functions of the unbiased Hamiltonian when they are shifted to n neighbouring periods [28],

$$\Psi_{\nu,l}(z) = \Psi_{\nu}(z - ld), \tag{2.12}$$

where d is the period length and l labels the period. Diagonalizing the biased Hamiltonian in the set of Wannier functions above yields the Wannier-Stark (WS) states (see Fig. 2.4). With the corresponding shifts in energy, the eigenvalue spectrum associated to the set of functions is completed. By constructing our eigenfunction basis as detailed above, orthogonality of the states within the neighbouring periods is preserved. The WS states are a basis of the biased QCL heterostructure, limited to the n neighbouring periods [28].

2.2.3 Carrier transport in QCLs

There exist several techniques to model transport in QCLs. These can be classified in increasing complexity and computational demand (see Fig. 2.5). In this subsection, a brief summary of these techniques is presented. A more detailed review of different modeling methods can be found in Refs. [10, 28, 39].

The simplest approach to carrier transport in QCLs is to use rate equations, which describe the time evolution of the electron population, $\dot{n}_\alpha$, in a subband α [10],

$$\frac{\partial n_\alpha}{\partial t} = \sum_\beta R_{\beta\to\alpha} n_\beta - R_{\alpha\to\beta} n_\alpha. \tag{2.13}$$

The transition rate at which an electron jumps from one subband α to another subband β, $R_{\alpha\to\beta}$, can be implemented *phenomenologically* by using empirical transition rates or through Fermi's Golden Rule [10]. Rate equations account for single-electron transitions between the electronic eigenstates of the heterostructure, yielding a *state-level* accuracy for the description of carrier transport in the device. It is important to remark that rate equations (2.13) disregard the electronic subband distributions in the transverse direction [39]. Then, a more advanced approach is to turn to the Boltzmann transport equation, where the in-plane motion of electrons is considered. The in-plane k-resolution enables the computation of both the α eigenstate occupation, n_α and in-plane electronic distribution, $f_\alpha(\boldsymbol{k})$, [10]

$$\frac{\partial f_\alpha(\boldsymbol{k})}{\partial t} = \sum_\beta \sum_{\boldsymbol{k}'} R_{\beta,\boldsymbol{k}'\to\alpha,\boldsymbol{k}}\, f_\beta(\boldsymbol{k}') - R_{\alpha,\boldsymbol{k}\to\beta,\boldsymbol{k}'}\, f_\alpha(\boldsymbol{k}), \tag{2.14}$$

where the energy level populations n_α,

$$n_\alpha = \frac{2}{A} \sum_{\boldsymbol{k}} f_\alpha(\boldsymbol{k}) \tag{2.15}$$

are easily recovered. The system of equations for $f_\alpha(\boldsymbol{k})$ in eq. (2.14) is usually solved using Ensemble Monte-Carlo (EMC) methods [10]. This numerical method involves sampling scattering events for a large ensemble of electrons where observables are obtained by averaging over the ensemble [10].

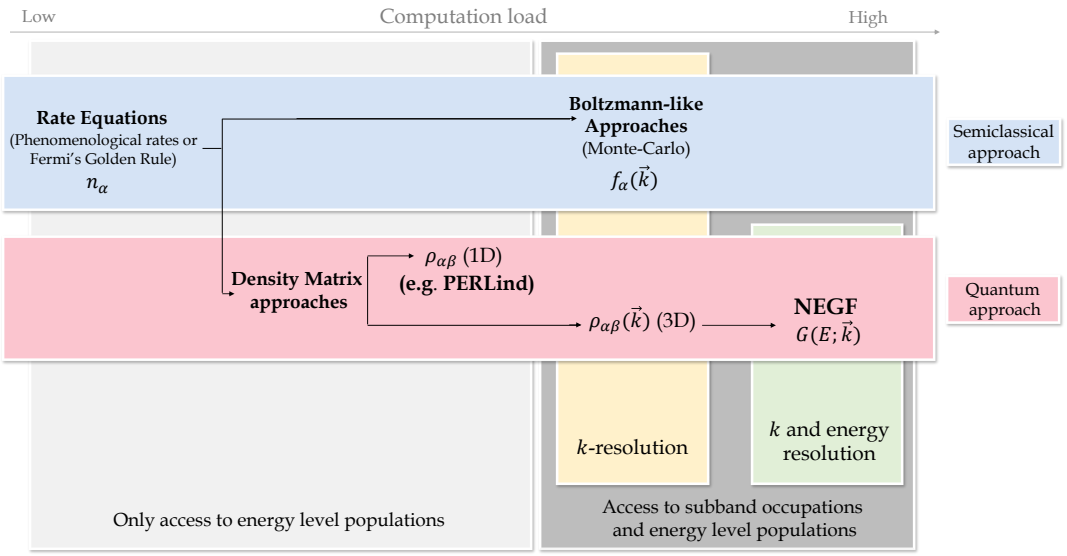

Figure 2.5: Diagram of approaches for transport in QCLs at different levels of accuracy.

Both rate equations and Boltzmann-like approaches are built upon a *"hopping transport"* scheme [10]: the scattering rates are constructed considering single-electron transitions between the eigenstates of the system. They are referred to as *semiclassical* approaches (see Fig. 2.5), since purely quantum effects such as *coherence*, state correlations and *dephasing* are not considered [39, 40]. States with coherences are superpositions of eigenfunctions of the system. If these states are neglected, the jumps between well-defined energy eigenstates occur instantaneously, without any coupling parameter or dephase. In the case of charged carriers localized at both sides of the injector barrier of the QCL active region, their tunnelling rate will only depend on the injection and extraction rates, independent of the barrier width. As no carrier bottleneck effects arise at the injector, the current density flowing through the QCL is overestimated [28, 39]. Therefore, a complete description of carrier transport in QCLs requires a coherent quantum theory to account for state broadening, tunneling and dephasing effects [40].

Quantum transport methods for QCLs include one (1D) and three (3D) dimensional density matrix approaches. These can be respectively regarded as an extension of the rate and Boltzmann-like transport equations above, where coherent states are incorporated in the non-diagonal elements of the density matrix [10]. In 1D density matrix methods, electrons jump from states $|\alpha\rangle$ to $|\beta\rangle$ and the state of the system is described by the density matrix $\rho_{\alpha\beta}(t)$. 3D density matrix methods go a step beyond and consider the transverse motion of electrons via $\rho_{\alpha,\beta}(\boldsymbol{k}, t)$. At this level, *quantum kinetics* are resolved. Quantum approaches based on NEGFs constitute a step further into complexity as they are k-resolved but they additionally contain *energy* resolution. NEGFs provide the most complete approach to non-equilibrium quantum transport as they allow for first principle calculations [27]. They have been successfully implemented for QCL simulation [25]. However, the method has a very large computational cost, which hinders its implementation in optimization algorithms to systematically search for improved QCL structures.

The approach to non-equilibrium carrier transport used in this thesis, PERLind, is a purely quantum, 1D density matrix approach (see Fig. 2.5). The formalism and its implementation for QCL simulation are introduced in full detail in Chapter 3.

Chapter 3 | Non-Equilibrium Quantum Transport

So far, we have reviewed the techniques available to model and simulate transport in QCLs. In this chapter, we focus on a density matrix method which can be used to describe non-equilibrium dynamics of an open system: the PERLind approach. The approach is implemented in the Lindblad-QCL (LQCL) Python package, discussed at the end of the chapter, to simulate QCLs.

3.1 Non-equilibrium quantum dynamics in open systems

A QCL is a composite of two systems in contact with each other: the electrons cascading down the structure, an *open* quantum system, and the semiconductor heterostructure, which acts as a reservoir and exchanges energy with the open system. The description of an open quantum system coupled to a bath or a reservoir is a long-standing problem in Physics. Its complexity resides in the interaction between the bath and the system. Transport phenomena in quantum dots or carrier dynamics in heterostructures are a few examples where this problem arises [26].

3.1.1 A density matrix approach

The first step to characterize the evolution of any quantum system is to account for its quantum states. For that purpose, we turn to the density operator, $\hat{\rho}$, which provides a statistical description of the state of a system. In a system where coherences and bath-induced dephasing are relevant [41], the density matrix ρ_{ij} enables a complete description of the full picture: the diagonal elements ρ_{ii} account for pure eigenstates of the Hamiltonian and provide the eigenstate populations, while the off-diagonal elements ρ_{ij} with $i \neq j$ constitute the coherences [26] that arise from the bath and a time-dependent Hamiltonian. The time-evolution of the density operator is given by the von-Neumann equation,

$$\frac{\partial \hat{\rho}(t)}{\partial t} = \frac{i}{\hbar}\left[\hat{\rho}(t), \hat{H}\right], \tag{3.1}$$

where $\hat{H}$ and $\hat{\rho}(t)$ are the Hamiltonian and density matrix operators, respectively, of the complete system (open quantum system and bath). Equation (3.1) can be further simplified by working with the reduced density matrix, i.e. by only considering the degrees of freedom in the open quantum system [26]. From now on, $\hat{\rho}$ will only refer to the open system. The total Hamiltonian $\hat{H}$ is the sum of two contributions: the reduced system Hamiltonian, $\hat{H}_S$, and the perturbation that constitutes the bath, $\hat{H}_{Bath}$,

$$\hat{H} = \hat{H}_S + \hat{H}_{Bath}. \tag{3.2}$$

3.1.2 Resolution of the von-Neumann equation

From equation (3.1), the time-evolution of the density operator in the $\hat{H}_S$ eigenstate basis $\{|a\rangle\}$ is often approximated by [26]

$$\frac{\partial \rho_{ab}(t)}{\partial t} = \frac{i}{\hbar}(E_b - E_a)\rho_{ab}(t) + \frac{i}{\hbar}\langle a|\,\hat{H}_{ext}(t)\,|b\rangle - \sum_{cd} K_{abcd}\rho_{cd}(t). \tag{3.3}$$

Here, E_a is the eigenvalue corresponding to the ket $|a\rangle$, $\hat{H}_{ext}(t)$ is any externally applied time varying field (e.g. the laser optical field) and K_{abcd} is the tensor that accounts for the system-bath coupling. It is important to emphasize once again that eq. (3.3) is an approximation: it is local in time; bath-induced memory terms $\rho(t - t')$ with $t' < t$ are ignored.

As it is common for most problems in Quantum Mechanics, the initial approach to eq. (3.3) is to apply perturbation theory under the assumption that the system-bath coupling is weak. Perturbation methods for quantum systems in contact with their environment were first introduced in references [42, 43] and lead to the Wangsness-Redfield-Bloch (WRB) equations. Although vastly employed, these equations entail a major physical problem: they yield negative occupation probabilities [26]. Positively defined occupation numbers are only guaranteed by the Lindblad-Gorini-Kossakowski-Sudarshan (LGKS) formalism [44, 45].

The LGKS mathematical formalism establishes that if the coupling between the open quantum system and the bath is described by a tensor K^{LGKS} such that the dynamical evolution of the reduced density operator is given by [26]

$$\frac{\partial \hat{\rho}}{\partial t} = \frac{i}{\hbar}[\hat{\rho}(t), \hat{H}_0] + \sum_j \Gamma_j \left(\hat{L}_j \hat{\rho} \hat{L}_j^\dagger - \frac{1}{2}\{\hat{\rho}, \hat{L}_j^\dagger \hat{L}_j\}\right), \tag{3.4}$$

then, the diagonal elements in the density matrix will be definite positive. In eq. (3.4), $\hat{H}_0$ includes the open system Hamiltonian and any external applied field, $\hat{L}_j$ is a jump operator associated to a microscopic system-bath coupling process j and Γ_j is a coupling constant. To guarantee positive occupation numbers and populations, the coupling tensor must have the structure of a Lindblad dissipator

$$K^{\text{LGKS}} \to \sum_j \Gamma_j \left(\hat{L}_j \hat{\rho} \hat{L}_j^\dagger - \frac{1}{2}\{\hat{\rho}, \hat{L}_j^\dagger \hat{L}_j\}\right). \tag{3.5}$$

Eq. (3.4) can then be solved to obtain the density matrix of the open quantum system.

3.2 The PERLind approach

The PERLind approach is a heuristic and phenomenological density matrix method that proposes a scheme for the construction of a Lindbladian dissipator as in (3.5) [26]. Therefore, it can be used to model quantum transport in out-of-equilibrium systems. The approach goes beyond other 1D density matrix approaches like the *secular approximation*, where bath induced coherences are neglected, as it is detailed in Ref. [46]. PERLind's versatility has been proved in applications on double-dot systems, the description of chemical transport in chromophores and quantum transport in QCLs [26].

3.2.1 Space and energy resolution

The PERlind approach relies on two factors: the resolution of the spatial and energy properties of the microscopic system-bath coupling. Transitions in the open quantum system depend on the location of the bath with respect to the reduced system. For instance, in a coupled double-dot in contact with two (left and right) reservoirs, it is relevant to specify from which reservoir carriers tunnel from. In QCLs, injection and extraction of electrons into the laser states depends on their localization. The energy distribution of the reservoirs is also decisive to model quantum transport as it determines the strength of the system-bath coupling and constrains the available transitions, effectively limiting quantum transport [26]. The PERLind approach proposes a scheme to construct a position and energy resolved Lindblad coupling tensor (3.5). The steps to implement the approach are described in detail in [26], section II. Here we present a short summary, but the interested reader is directed to the reference for further details.

The first step in PERLind is to identify the mechanisms that drive quantum transport in the device and associate an operator to them. The main coupling processes in the bath are modelled by a jump operator $\hat{L}_j$, where j denotes the scattering mechanism. The operator will be accompanied by a function $f_j(E)$ that contains information about the energy of the transition. These jump operators $\hat{L}_j$ are represented in the eigenfunction basis $\{|\psi_i\rangle\}$ of the open system hamiltonian $\hat{H}_S$,

$$L^j_{\alpha\beta} = \langle\psi_\alpha|\,\hat{L}_j\,|\psi_\beta\rangle\,. \tag{3.6}$$

To build the Lindblad tensor, we define the $\tilde{L}_{\alpha\beta}$ matrix element, where the energy dependence of the approach is added through an energy-dependent function $f_j(E)$

$$\tilde{L}^j_{\alpha\beta} = L^j_{\alpha\beta}\sqrt{f_j(E_\beta - E_\alpha)}. \tag{3.7}$$

The square root in equation (3.7) is phenomenologically justified for it allows Fermi's Golden Rule for the scattering rate to be recovered through

$$R^j_{\alpha\to\beta} = |\tilde{L}^j_{\beta\alpha}|^2 = |L^j_{\beta\alpha}|^2 f_j(E_\beta - E_\alpha). \tag{3.8}$$

Eq. (3.8) provides the rate of the j-th scattering process and it is coincident with the experimentally measured rates. The Lindbladian dissipator that arises from the PERLind approach is

$$K^{\text{PERLind}}_{abcd} = -\sum_j \left(\tilde{L}^j_{ac}\tilde{L}^{j\star}_{bd} - \frac{1}{2}\sum_e \tilde{L}^{j\star}_{ed}\tilde{L}^j_{eb}\delta_{ac} - \frac{1}{2}\sum_e \tilde{L}^{j\star}_{ea}\tilde{L}^j_{ec}\delta_{bd}\right), \tag{3.9}$$

which conserves the same structure as the dissipator in (3.5). By inserting the above tensor in (3.3), the expression turns into an LGKS master equation, guaranteeing the positivity of the occupation numbers. The solution of equation (3.3) in the stationary limit (i.e. $\partial\hat{\rho}/\partial t = 0$) with the Lindblad coupling tensor (3.9) provides the steady-state density matrix operator of the open system.

3.2.2 The PERLind approach for QCLs

As we have just seen, the PERLind approach proposes a scheme to model quantum transport in open systems in contact with the environment. Therefore, it can be used as the theoretical basis for transport simulations in QCLs [26]. To do so, we must identify the relevant scattering mechanisms that drive transport in the device. As it has already been discussed in section 2.1, the major scattering processes associated to the QCL heterostructure are LO-phonon scattering, impurity scattering and IFR scattering. Carrier-carrier interactions are also of relevance but have not been considered in this work. The detailed construction of the Lindblad dissipators within the PERLind scheme for LO-phonon, impurity and IFR scattering can be found in appendices A, B and C.

3.3 QCL observables

The density matrix of the system is the key quantity to extract the measurable observables of a QCL: optical gain and current density at applied bias. The operation of a QCL is characterized by the (DC) current-voltage curve (I-V) and the gain spectrum with its corresponding peak. The current density is given by [26]

$$J(z) = \frac{-2e}{A} \sum_{\boldsymbol{k},\alpha\beta} \mathrm{Re}\left(\rho_{\beta\alpha}(\boldsymbol{k}) \psi^{\star}_{\alpha}(z) \frac{\hbar}{m_c(z) i} \frac{\partial \psi_{\beta}(z)}{\partial z} \right), \tag{3.10}$$

where Re denotes the real part of the expression, e is the fundamental unit of charge, A is the trasversal section of the device and $m_c(z)$ is the effective mass. It is important to note here that the current density depends on the averaged density matrix,

$$\rho_{\alpha\beta} = \frac{2}{A} \sum_{\boldsymbol{k}} \rho_{\alpha\beta}(\boldsymbol{k}). \tag{3.11}$$

Hence, the current density flowing in the device can be computed within a 1D density matrix approach.

The computation of the laser gain requires a dynamical solution. Therefore, time is now introduced in the calculations. The application of a time-varying AC field to the gain medium allows us to obtain the gain spectrum. The AC field can be modelled by a time-dependent oscillating function such as

$$F(t) = F_{AC} \cos(\omega t), \tag{3.12}$$

where ω is the frequency at which the AC field oscillates. The $F(t)$ field moves charges in one QCL period, forcing them to oscillate with frequency ω. As a result, an oscillating current arises, which, together with the DC current in eq. (3.10) gives [26]

$$J(t) \approx J_{DC} + J_{\cos} \cos(\omega t) + J_{\sin} \sin(\omega t). \tag{3.13}$$

For sufficiently large AC fields, the *transparency condition* is reached: the oscillating field yields an equal distribution of carriers in the ULS and the LLS, which ends population inversion and consequently, stimulated and spontaneous emission. In this thesis, the optical gain spectrum is given by the real part of the current in (3.13) [26],

$$g(\omega) = -\frac{J_{\cos}}{F_{ac}\sqrt{\epsilon_r}\epsilon_0 c}. \tag{3.14}$$

For more details about this calculation, see [3] (section 2.9). When gain is above the loss threshold g_{TH}, laser operation in the QCL begins. This means there are more photons emitted than absorbed in the cavity, mirror and waveguide. These constitute the device *losses* and establish g_{TH}. Fully characterizing the QCL requires determining the current density at threshold, J_{TH}, which is the current density value at which $g = g_{\mathrm{TH}}$. In this thesis, gain threshold is assumed constant, although in reality it depends on factors like temperature and the shape and materials of the laser cavity [27].

The AC field has two main effects on the perfomance of a QCL. First, it provokes an increase in the current density after laser ignition. This happens because the oscillating field pushes carriers down the structure. Consequently, population inversion is rapidly lost. Thus, the AC field is linked to a decrease in gain. Gain decreases before saturating at the threshold value. At this point, the electric fields in the device self-consistently recover gain from further losses. Such phenomenon is known as *gain clamping* or *gain saturation* [3]. The value of $F(t)$ for which $g = g_{TH}$ marks the laser operation point.

3.4 The LQCL package

The LQCL package is a Python computational module that implements the PERLind approach to simulate transport in QCLs [26]. It builds a Lindblad coupling tensor (3.9) for LO-phonon and impurity scattering by identifying energy and space resolving elements, L^q_{ab} and $f_q(E_b - E_a)$ of the mechanisms (see Appendices A and B). Once the dissipator is constructed, the package solves the corresponding LGKS master equation (3.3) and obtains the reduced density matrix $\hat{\rho}$ in the stationary regime, i.e. $\partial\hat{\rho}/\partial t = 0$. LQCL provides two relevant observables to characterize the performance of a QCL: the current density for the applied bias, as given by (3.10), and optical gain (3.14). State populations can be inferred from diagonal elements of $\hat{\rho}$.

LQCL is a self-consistent simulation package: it only inputs well-known material parameters like the effective mass or the band gap energies at the Γ point, as well as the active region dimensions, i.e. barrier and well widths and alloy fractions of the materials. There is no fit of other kind [26]. The package inputs the eigenstates of the heterostructure from a Fortran module that computes WS states as described in section 2.2. The initial version of the LQCL package (which will be used throughout the preliminary simulations) considers a single input temperature, which is used both as an electronic T_E and lattice T_L temperatures. We will refer to it as $T_{\mathrm{Simulation}}$ in Chapter 4.

The package provides a current density value for every bias point (I-V curve), as well as the gain spectrum for non-zero AC field. The simulations are run in a *swipe up* from lower to higher bias, where the bias step size can be determined by the user. The choice of the step size can be crucial to resolve resonances, as will be discussed in Chapter 4. To identify the operation point, the simulations are first run at a low AC field ($\sim 10^{-3}$ meV) and at a range of frequencies centred around the experimental emission frequency. The current density at threshold, J_{TH}, is determined when $g = g_{TH}$. The frequency at which the laser operates is located at the peak of the simulated gain spectrum with $g > g_{TH}$. As the AC field is increased, gain decreases until $g = g_{TH}$ is recovered. This point, defined by an applied DC voltage and an external AC optical field, constitutes the operation point of the laser.

Chapter 4 | Results and Discussion

In this chapter, we present and discuss the tests performed on the LQCL Python package. We start the chapter with a brief overview of the simulation results. Next, we discuss the general features of the I-V curves and gain spectra obtained with LQCL. The chapter continues with a discussion on the role of temperature in the simulations. We close the chapter with the implementation of IFR scattering in LQCL.

A general remark on the comparison to experimental values

Our LQCL validity test consists of a quantitative comparison of the simulation results with published experimental data. The comparative approach we have taken is similar to the recently published work in [27]. The QCLs simulated in this thesis were found in the literature and hence, developed in different laboratories worldwide. Therefore, the experimental values are biased with respect to their growth source [47]. Besides, LQCL solely simulates the active region of the laser. In our simulations, the waveguide and cavity, which do have an impact on the experimental data, are not considered; they are only introduced as an estimated loss coefficient in the gain spectra.

Experimental values are measured at *heatsink temperature*, T_{Heatsink}, the experimental temperature at which data is gathered in the laboratory. This temperature is different from the lattice and electronic temperatures we input in the LQCL code. Such difference is difficult to quantify; we can only provide a justified estimation of it for continuous wave (cw) and pulsed mode operation of the laser. Thus, although LQCL is aimed to simulate transport in QCLs as accurately as possible, some intrinsic factors will hinder an exact comparison of our results with the experimental data. However, the ultimate goal of our simulation method is to study different active regions at a reduced computational cost within a *"simplified yet physically meaningful"* framework [48].

4.1 Testing the LQCL package: Simulations of QCLs in the THz and IR

In order to test the LQCL package, we have focused on simulating exemplary QCL devices. These devices can be found in [14, 16, 17, 22, 38, 49, 50, 51] and [15, 52, 53] for THz and IR-QCLs, respectively. This QCL selection was motivated by the purpose of testing LQCL for the main active region designs [4, 20]. These devices stand out because of their innovative injection and extraction mechanisms or as a result of the records established by their performance. Such is the case for Fathololoumi *et al.*'s device [16], which currently holds the published record $T^{\text{max}}_{\text{Heatsink}} = 199.5$ K for THz-QCLs, or that developed by Li *et al.* [50] exhibiting very high output powers. The above set of devices ensures a sufficiently large test space to gather conclusions about LQCL's scope.

We have found that the LQCL package provides results that are predictive at a *qualitative* level. The shape of the I-V curves can generally be reproduced from experiment. We are able to observe parasitic currents and tunneling resonances. Laser gain is obtained close to the design bias of the devices. Furthermore, the peaks of the emission spectra agree well with experimental frequencies. Nevertheless, the package does not provide good *quantitative* results. We have observed a generalized underestimation of the current density at high applied bias. The simulated threshold, J_{TH}, and maximum current densities, J_{max}, are below experimental values. Besides, the package provides unphysical negative currents and the I-V curve shows unexpected jumps and peaks that might be of computational nature. All these results will be discussed in detail below and examples illustrating them will be provided.

4.2 The I-V curve

The current-bias (I-V) curve constitutes the first validity check for LQCL. As Callebaut *et al.* point out in [54]: *"(...) only when the simulation produces current densities consistent with experiments can we have confidence in other calculated results, such as subband populations and gain"*. Therefore, we start our test of the LQCL package by checking whether the main features of the experimental I-V curves (i.e. resonances, current density at threshold or maximum current density) are also obtained in the simulations.

As we have mentioned before, it is possible to observe tunneling resonances in the I-V curve with LQCL. These resonances, which stem from the alignment of different energy levels in the QCL, appear as peaks in the I-V curve [19]. In Fig. 4.1, we present the results of the simulations for a THz-QCL where extraction and injection are assisted by phonons, designed by Dupont *et al.* [22]. In plots (a) and (b) of the figure, we show the I-V curve for this device, together with experimental data. The *"shoulders"* in plot (a) at 16 mV/period and 31 mV/period, marked with two arrows, signal the alignment of the extractor with other two laser levels at the indicated biases (see Fig. 1 in [22]). These alignments are marked with dashed lines in the experimental curve in plot (b) at 6 V and 9 V. The simulations also predict a Negative Differential Resistivity (NDR) region. In such regions, an increase in the bias produces lower currents. In Fig. 4.1 (a), we observe an NDR region extending from 32 mV/period to 49 mV/period; the current then increases and recovers the value it had before the NDR region at 60 mV/period. This agrees well with the experimental curve, where we see a plateau extending from 8.4 V (30 mV/period) to 18.2 V (65 mV/period), after subtracting a Schottky drop of 0.8 V from the voltage [22]. The simulated current density peak at 76 mV/period coincides with the design bias of the device (21 V). In Fig. 4.1 (d), we compare the experimental and simulated J_{TH} of the device. The simulated data is shifted right to higher temperatures and down to lower current densities. This shift signals an underestimation of J_{TH} of ~ 400 A/cm^2 with respect to Dupont *et al.*'s experimental data [22] (relative error of $\sim 40\%$). A summary of the main features discussed above can be found in Table 4.1.

In Fig. 4.2 we present the results of the simulations for a different THz-QCL designed by Fathololoumi *et al.*, that operates at high temperatures (~ 200 K) [16]. In plot (a) of the figure, we are able to see a tunneling resonance at 39 mV/period. This sharp peak is coincident with the theoretically expected alignment of the injector and extractor levels

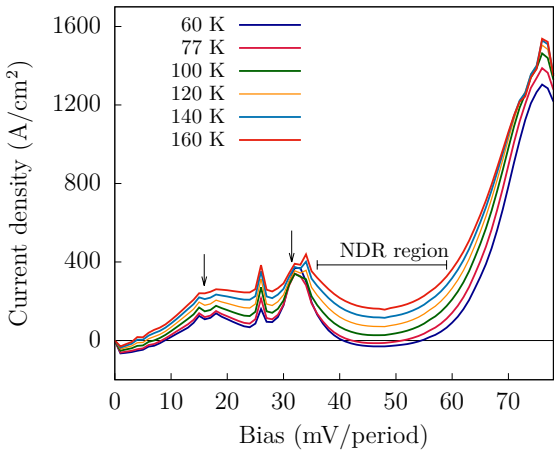

(a) Simulated I-V curve.

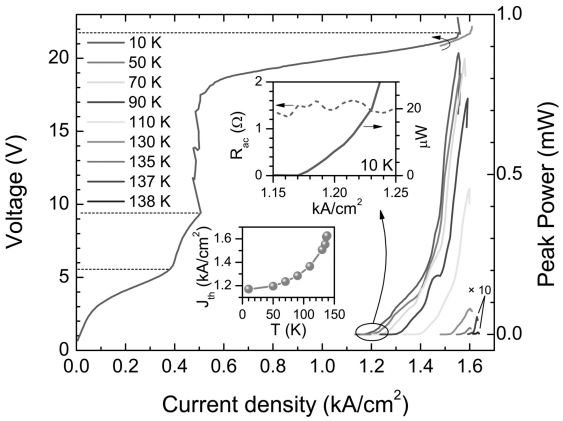

(b) Experimental data.

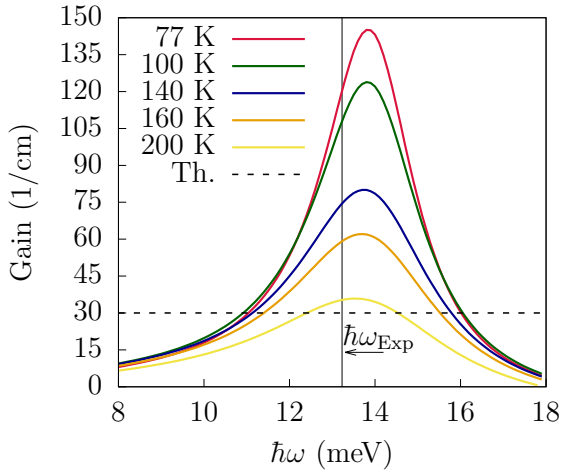

(c) Simulated gain spectra.

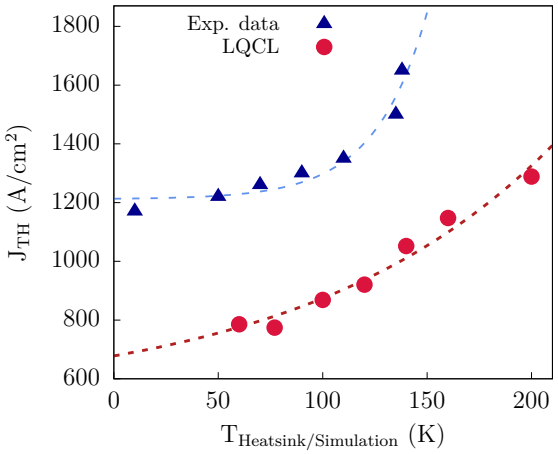

(d) J_{TH} as a function of temperature.

Figure 4.1: Data for Dupont *et al*'s THz QCL [22]. (a) Simulated I-V plot for $T_{\mathrm{Simulation}} \in [60, 140]$ K. The downward pointing arrows indicate two tunneling resonances due to the alignment of the extractor state with two different laser levels. There is a Negative Differential Resistivity (NDR) region and subsequent recovery of J between biases $\sim 31 - 60$ mV/period. (b) Experimental data. The design bias of the structure is 76 mV/period (21 V) and the device exhibited a maximum operating temperature of $T^{\mathrm{max}}_{\mathrm{Heatsink}} = 138$ K. The figure was taken from [22]. (c) Simulated gain spectra of the device for several simulation temperatures. The experimental frequency, $\nu_{\mathrm{Exp}} = 3.2$ THz, is marked with an arrow. (d) Current density at threshold J_{TH} as function of temperature for experimental (triangles) and simulated (dots) data. The experimental data is gathered at T_{Heatsink}, while the simulation data is obtained at $T_{\mathrm{Simulation}}$. Data is fitted to an exponential function $J_{TH} = J_0 e^{T/T_0}$, where $T_0 = 30$ K for the experimental data (blue dashed line) and $T_0 = 110$ K for LQCL (red dashed line).

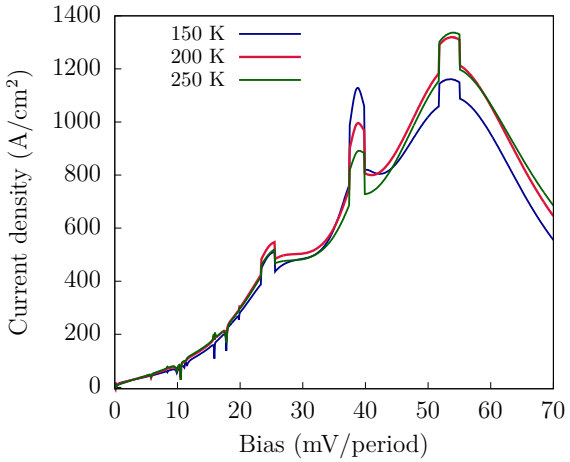

(a) Simulated I-V curve.

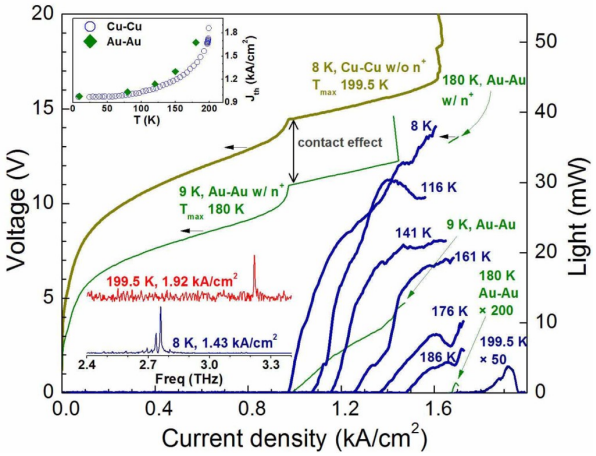

(b) Experimental data.

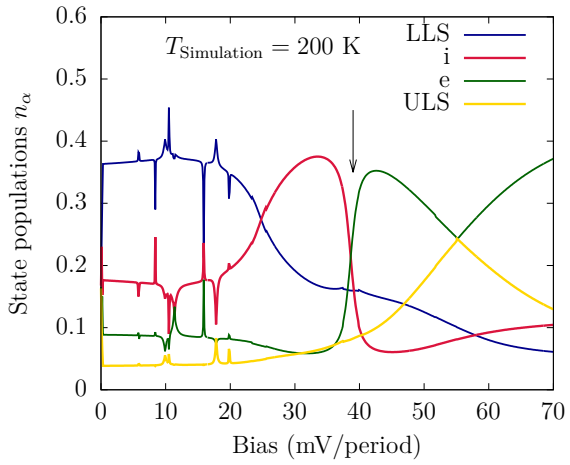

(c) Simulated laser level occupations.

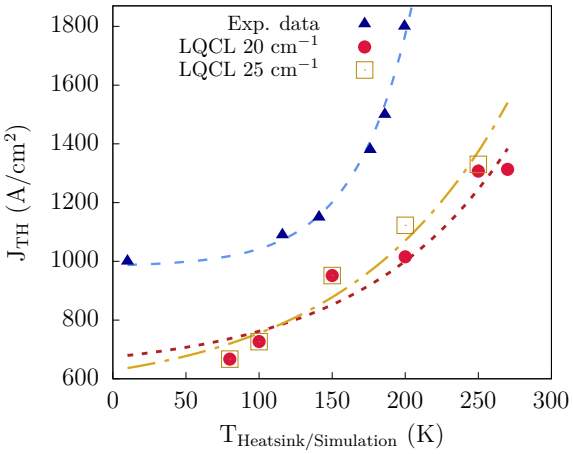

(d) J_{TH} as a function of temperature.

Figure 4.2: Data for Fathololoumi *et al*'s THz-QCL [16]. (a) Simulated I-V curve for $T_{\text{Simulation}} = 150, 200$ and 250 K. At 39 mV/period, the i-e alignment resonance peak can be seen. (b) Experimental data. The design bias of the structure is 50 mV/period and it experimentally operates until $T^{\text{max}}_{\text{Heatsink}} = 199.5$ K. Figure taken from [16]. (c) Normalized populations of the WS levels as a function of the applied bias. The ULLS, LLS, i and e are shown. A downward pointing arrow marks the alignment of the injector and the extractor. Population inversion occurs above 45 mV/period. (d) Experimental and simulated data for J_{TH} as a function of temperature for $g_{TH} = 20$ cm^{-1} (red dot) and 25 cm^{-1} (gold box). Experimental values are gathered at heatsink temperature T_{Heatsink} and the simulated data at $T_{\text{Simulation}}$. The fits correspond to an exponential function $J_{TH} = J_0 e^{T/T_0}$, where $T_0 = 39$ K for the experimental fit (blue dashed line), as given in [16], $T_0 = 100$ K for $g_{TH} = 20$ cm^{-1} (red dotted line) and $T_0 = 110$ K for $g_{TH} = 25$ cm^{-1} (gold dashed line).

Table 4.1: Summary of the main I-V curve features identified during the simulation of Dupont *et al.*'s THz-QCL [22], compared to experimental data.

Feature	LQCL	Experiment
Resonant alignment n. 1 (mV/period)	16.0	18.0
Resonant alignment n. 2 (mV/period)	31.0	29.0
NDR and recovery region (mV/period)	[32 : 60]	[30 : 65]

at 8.9 kV/cm ($\sim$ 39.2 mV/period). Such alignment is discussed by Fathololoumi *et al.* in [16] and it can be observed at $\sim$ 10 V in the experimental plot for the Au-Au device (Fig. 4.2, b). The evolution of the laser level populations with applied bias confirms the injector-extractor alignment at 39 mV/period and shows that population inversion starts slightly above the resonance, with the crossing of the ULS and the LLS at $\sim$ 47 mV/period (Fig. 4.2, c). The comparison of the simulated J_{TH} as a function of temperature with experimental values in Fig. 4.2 (d) points out the aforementioned current underestimation in the simulations; we see that LQCL's predictions are on average 250 A/cm^2 below experimental data for this THz-QCL design (relative error of $\sim$ 25%). We must also note that Fathololoumi *et al.* indicate a maximum current density of J_{max} =1450 A/cm^2 [16]. The simulated current density in plot (a) does not reach this value for any of the $T_{\mathrm{Simulation}}$ temperatures.

So far, we have shown that LQCL correctly identifies resonant peaks in the I-V curves. Examples of that were the *"shoulders"* in Dupont *et al.*'s device (Fig. 4.1) and the tunneling peak in Fathololoumi *et al*'s device (Fig. 4.2). However, the underestimation of J_{max} and J_{TH} appears as a recurrent feature in the simulations, with $\Delta J_{\mathrm{TH}} = J^{\mathrm{TH}}_{\mathrm{Experiment}} - J^{\mathrm{TH}}_{\mathrm{Simulation}} \approx 400$ A/cm^2 for Dupont *et al*'s device (Fig. 4.1, d) and $\Delta J_{\mathrm{TH}} \approx 250$ A/cm^2 for Fathololoumi *et al*'s device (Fig. 4.2, d). Another example is presented in Fig. 4.3, where we show the data for Han *et al*'s D2 THz-QCL design [17]. In [17], authors report three *"step increases"* of the current density to 0.2 kA/cm^2, 0.32 kA/cm^2 and 1.2 kA/cm^2 (see Fig. 4.3, b). These steps signal parasitic currents, which are alternative paths for the transport of carriers in the active region of a QCL. Parasitic currents appear when energy levels that do not constitute the main transport path[1] align. The three experimental data points in Fig. 4.3 (a) locate those parasitic currents in our simulations (after extracting at the contacts a drop of 2.5 V for this device [17]). In plot (a) of the figure, the double-head arrow at 50 mV/period signals the disagreement between the simulated curves and the parasitic current at high bias (relative error of 50%). In this case, the simulated current is $\sim$ 600 A/cm^2 below the experimental data point. Our results also indicate an NDR region at high bias (>45 mV/period), which cannot be seen in the experimental curve (Fig. 4.3, b). In the low bias region (<30 mV/period), the two experimental points at 7.5 mV/period and 21 mV/period agree well with our simulations. These results show that we are able to resolve the two parasitic currents at low bias, but we fail to see the third parasitic current at high applied bias due to the underestimation of the current flow.

[1] i $\rightarrow$ ULS $\rightarrow$ LLS $\rightarrow$ e

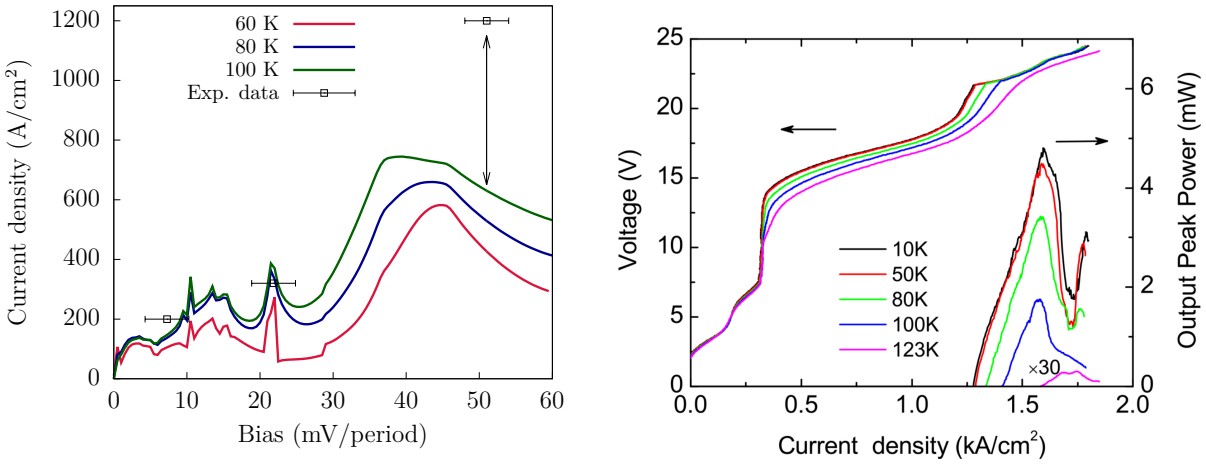

(a) Simulated I-V curve.

(b) Experimental data.

Figure 4.3: Data for Han *et al.*'s D2 THz-QCL [17]. (a) Simulated I-V curve for $T_{\text{Simulation}} =$ 60, 80 and 100 K. Three experimental parasitic currents are marked with black boxes, where an error bar has been added to account for a calibration of 2.5 V discussed by authors [17]. Only three WS states were used in the simulation. (b) Experimental L-I-V curve for the same device at different heatsink temperatures. The design bias of the structure is 60 mV/period and it experimentally operates until $T^{\text{max}}_{\text{Heatsink}} = 123$ K. Figure taken from [17].

4.2.1 Spikes in the I-V curve

At very low applied bias (<15 mV/period), we see that the shape of the I-V curve in Fig. 4.3 (a) is quite complex: it is full of spikes and it contrasts with the smooth curve measured in experiment (Fig. 4.3, b). The clean peak at 21 mV/period in the simulations can be identified as a parasitic current, according to the discussion above. However, it is difficult to distinguish whether other peaks that arise between 8 mV/period and 15 mV/period signal actual physical phenomena or stem from computational problems. These seemingly spurious peaks are not an isolated case: we can also observe a sharp peak at 25 mV/period in the I-V curve for Dupont *et al.*'s QCL (Fig. 4.1, a), and at 25 mV/period and 52 mV/period for Fathololoumi *et al.*'s QCL (Fig. 4.2, a). Furthermore, in a recently published article [27], Burnett *et al.* present THz-QCL simulations using a k-resolved density matrix approach, where they also observe spikes in their I-V curves similar to ours. It must be noted that this feature appears more prominently in our simulations. In the precedent section, we have argued that LQCL correctly predicts parasitic currents and tunneling resonances: the I-V curve exactly peaks where these alignment phenomena are experimentally reported and theoretically expected. However, we find no justification for the rest of the spikes in the curves. Therefore, in this section we will analyze the origin of these spikes to be able to discriminate them from actual physical phenomena.

To study the origin of the spikes and peaks in the I-V curve, we have repeated our simulations with a few modifications. First, we have reduced the bias step size to isolate spurious data points from the main I-V curve. Second, we have shifted in δ the centre of the QCL module from $z = d/2$ to $z = d/2+\delta$, where d is the length of a module. When we compute the WS states of the structure in the simulations, we classify them into different periods. This depends on the distribution of their probability density around the centre of the module. By shifting the centre of the module, we can modify how the energy levels

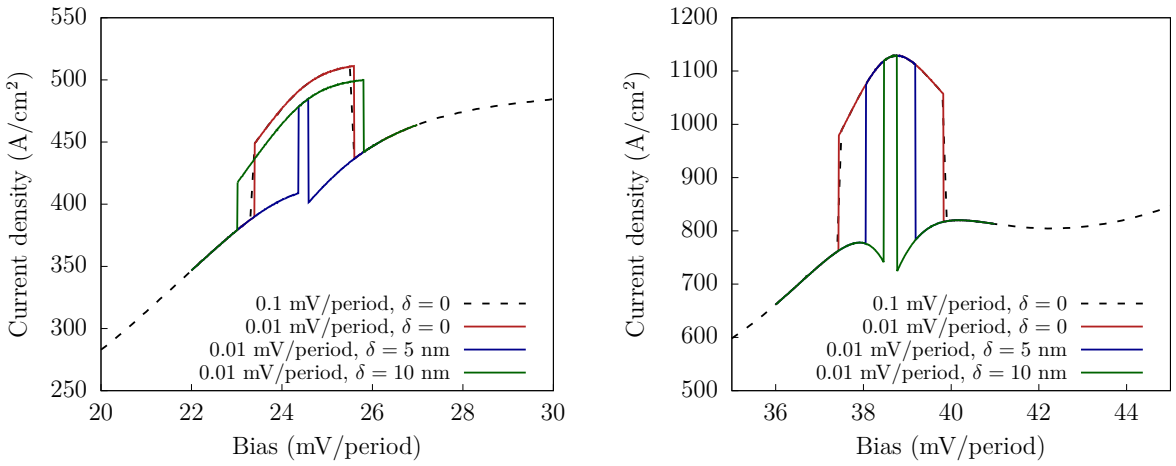

Figure 4.4: Detailed plots of two of the peaks in Fig. 4.2 for Fathololoumi *et al.*'s THz-QCL [16]. The black dashed line shows the I-V curve with a bias step size of 0.1 mV/period and no shift $\delta = 0$ nm. The red solid line indicates a change in the bias step size to 0.01 mV/period. For the blue solid line and green solid line the bias step size is the kept at 0.01 mV/period but the centre of the period is shifted $\delta = 5$ nm and 10 nm, respectively. (a) Peak centred around $\sim$ 25 mV/period. (b) Peak centred around $\sim$ 39 mV/period.

are classified into different periods. An example is shown in Fig. 4.5; here, we have only coloured the set of WS levels that the package classifies as within the central period; levels in neighbouring periods are shown in grey. Comparing plots (a) and (b) in the figure, we observe that we colour different WS levels depending on the position of the centre of the module: the blue level in plot (a) becomes the red level in plot (b), and the package colours with blue in (b) a level that belonged to a neighbour period in (a). In Fig. 4.4 we show the effect of shifs $\delta = 5$ nm and $\delta = 10$ nm on two of the peaks at Fathololoumi *et al.*'s I-V curve (see Fig. 4.2). Here, we observe that these peaks change shape depending on δ, which shows that they are linked to how the WS levels are classified into different periods (central period, first neighbours, etc...). This shows that a peak arises whenever we have a change in the set of WS states of a period. Such change is likely to occur at a resonance between two levels, where the states extend over a large range in space.

A QCL is a periodic structure where the basic module is repeated 30-200 times along the growth direction. Hence, the energy levels in neighbouring modules, which are extended, are equivalent and the laser observables should be independent of our WS basis choice; that is, the shift δ should not alter the results. However, in our simulations we consider a finite number of modules and impose boundary conditions to compute $\hat{\rho}$. This means that the number of neighbours included in the simulations plays an important role, specially at those operation points where levels align in resonance, as this might mean that we have a change in the coloured set of WS states as discussed above. Take plots (a) and (b) in Fig. 4.5 as an example. Suppose we limit our calculations to first neighbours. Then, the package only considers transitions between the levels in the central period (coloured) and neighbouring periods (grey). When we increase the bias, the levels cross and displace in energy. If, for a given bias, a change in the set of WS states occurs and thus, we colour different levels, we will also be considering different electronic transitions. For instance, in plot (a), the blue level is aligned with the red level; in plot

(b), the blue level is identified differently, as as one of the levels that was grey in plot (a). This has very important consequences: *First neighbour* boundary conditions in plot (b) are actually *second neighbour* conditions for the set of WS states in (a). Looking at plot (b), we now have transitions from levels in the left neighbouring period to the blue state, which was a grey level in the right neighbouring period in plot (a); that is, we have a transition between two formerly grey states, second neighbours. Thus, the peaks should reduce if more neighbours are included in the simulations. This is confirmed in Fig. 4.6 (a), where the peak at 24.5 mV/period flattens when second neighbours are considered.

4.2.2 Underestimation of the current density

As we have already discussed, the main discrepancy between the results of our simulations and the experimental curves is a generalized underestimation of the current density. Such underestimation is manifested in the values for $J_{\mathrm{TH}}^{\mathrm{Simulation}}$, which are between 200 A/cm^2 and 600 A/cm^2 below experimental data (Fig. 4.1 (d) and Fig. 4.2 (d)). In the simulations, our input temperature $T_{\mathrm{Simulation}}$ is expected to be higher than T_{Heatsink}. If there were no underestimation, the simulated curves for J_{TH} as a function of temperature should appear shifted right towards higher temperatures, yielding the same J_{TH} values for different T_{Heatsink} and $T_{\mathrm{Simulation}}$. Such shift between the curves would allow us to estimate the difference between both temperatures for pulsed mode and cw operation of the device. Nevertheless, as it can be seen in Fig. 4.1 (d) and Fig. 4.2 (d), the simulated curves are shifted diagonally, to the right and down, towards lower currents. They do not yield the same J_{TH} for different T_{Heatsink} and $T_{\mathrm{Simulation}}$. This signals the underestimation. The current underestimation is also particularly significant at high applied bias, where the values for J^{max} reported in experiment are never reached. In Fig. 4.7, data for Bismuto *et al.*'s mid-IR is shown [52]. In plot (a), we see that our simulation stops at $J_{\mathrm{max}} = 3$ kA/cm^2 while experimentally, maximum currents of 4 kA/cm^2 are reported (see plot b). This means our simulated J_{max} is 1 kA/cm^2 below experiment.

It must be remarked in the low bias region, the simulated current densities are not far from the experimentally reported values. Our (quantitatively) best simulated results correspond to a device operating at low biases designed by Mahler *et al.* [49]. For this device, authors report $J_{TH}^{\mathrm{Experiment}} = 75$ A/cm^2 at $T_{\mathrm{Heatsink}} = 10$ K and design bias of 21.76 mV/period (1.6 kV/cm) [49]. With LQCL, we obtained $J_{TH}^{\mathrm{Simulation}} = 70.77$ A/cm^2 at $T_{\mathrm{Simulation}} = 60$ K and 20.0 mV/period, where it is reasonable to assume that T_{Heatsink} is ∼30-60 K below lattice temperature during cw operation. These results support the hypothesis that the discrepancy between experimental and simulated current density is constrained to the region of high bias. Moreover, they suggest that the current underestimation must have its origin in a phenomenon linked to a large voltage drop or heating effects.

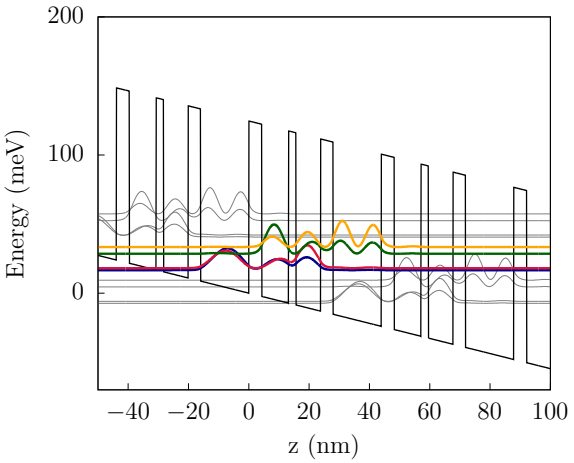

(a) 24 mV/period, no shift.

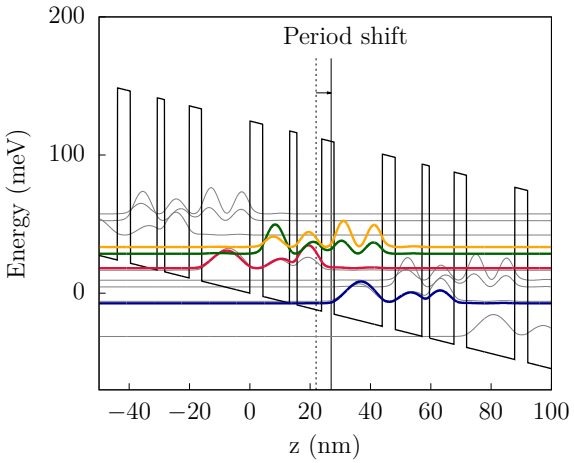

(b) 24 mV/period, $\delta = 5$ nm.

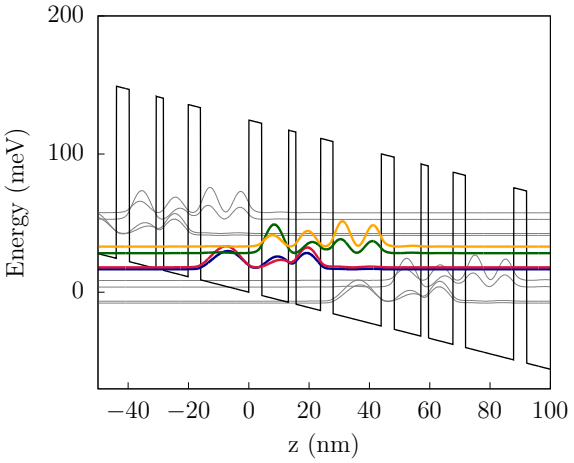

(c) 24.5 mV/period, no shift.

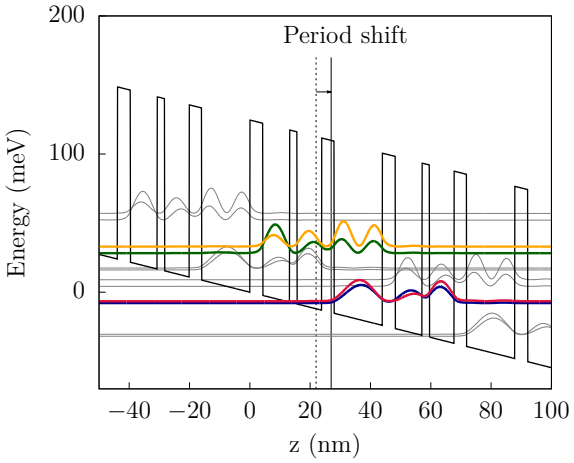

(d) 24.5 mV/period, $\delta = 5$ nm.

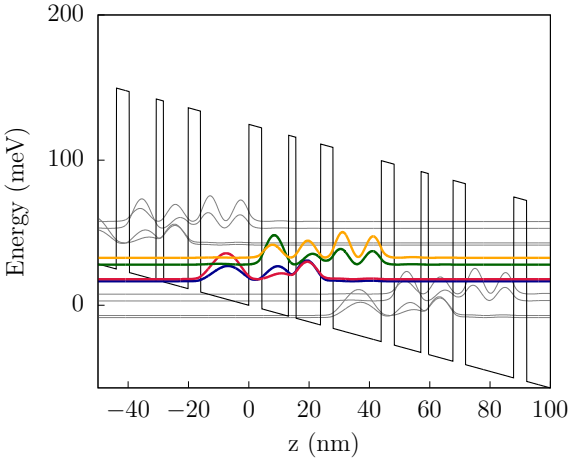

(e) 25 mV/period, no shift.

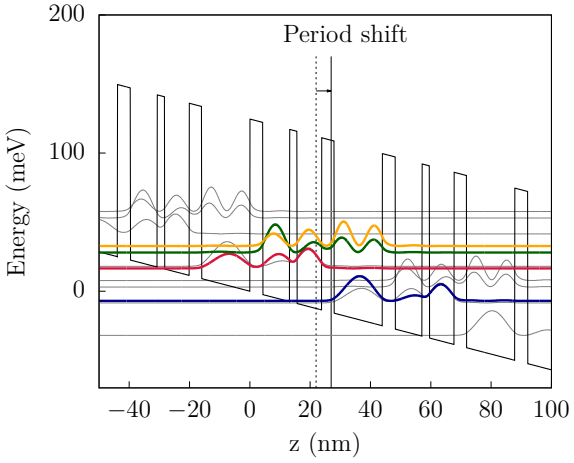

(f) 25 mV/period, $\delta = 5$ nm.

Figure 4.5: WS states for the THz-QCL in [16] at different applied biases without (left column) and with (right column) a shift of the centre of the period. The states in the central period ($d = 43.91$ nm) are shown in colour; levels in neighbouring periods are shown in grey. Only four WS states are considered per period.

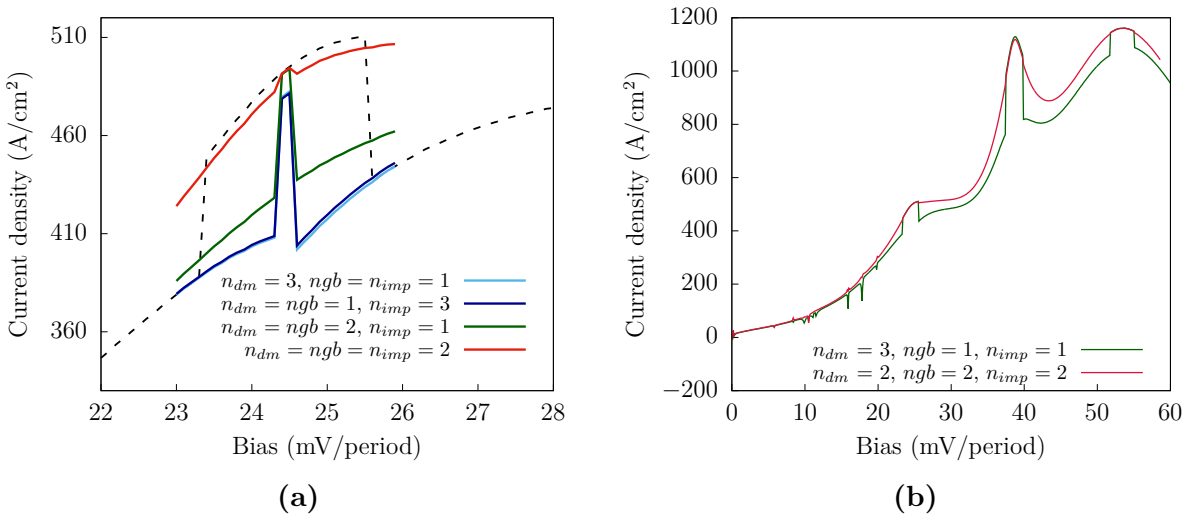

(a) **(b)**

Figure 4.6: (a) Detailed plot of the I-V curve peak at 24.5 mV/period for Fathololoumi *et al.*'s device in [16]. The black dashed line shows the I-V curve with a bias step size of 0.1 mV/period and no shift. The rest of the curves have been obtained with a step size of 0.01 and $\delta = 5$ nm; n_{dm} indicates the number of periods considered as the central period, ngb controls the neighbours included for LO-scattering and n_{imp} the neighbours included for impurity scattering. (b) I-V curve for Fathololoumi *et al*'s THz-QCL [16] at different levels of accuracy.

At high biases, the underestimation of the current density can be due to the following factors: neglecting the continuum states in our simulations, missing a scattering mechanism in the construction of the Lindblad dissipator or ignoring heating effects in the heterostructure. We have observed that ignoring the WS states that leak into the continuum is beneficial for the simulations, for it yields a smoother I-V plot and helps avoid the aforementioned current peaks and spikes. However, these states might play a role in dissipating the heat of the lattice with carriers jumping to the continuum. In fact, their effect on quantum transport might not be negligible, as believed [17]. In Fig. 4.6 (b) we observe that extending the simulation to more neighbours also increases the current density ~ 100 A/cm^2. As we have argued above for the origin of the peaks, this is because we are now considering more transitions that contribute to transport. A discussion on the role of heating requires a thorough review on temperature; hence, it be postponed to section 4.5.

Current can also be underestimated because LO-phonon and impurity scattering, the only mechanisms implemented in LQCL, might not be enough to account for the relevant carrier dynamics in a QCL. This could explain the low J_{TH} values we simulate. The lack of scattering phenomena degrading the performance of the device enables laser operation at low currents. Carriers find few *obstacles* (i.e. elastic and inelastic scattering mechanisms) along the heterostructure that could potentially hinder laser operation. Additional scattering mechanisms such as carrier-carrier interactions and IFR scattering can drive the current up and set a higher threshold for laser operation. With this in mind, we decided to implement IFR scattering in the LQCL code via the PERLind approach (see 3.2.2 and Appendix C). The results obtained by including IFR in the simulations will be shown and discussed in section 4.7.

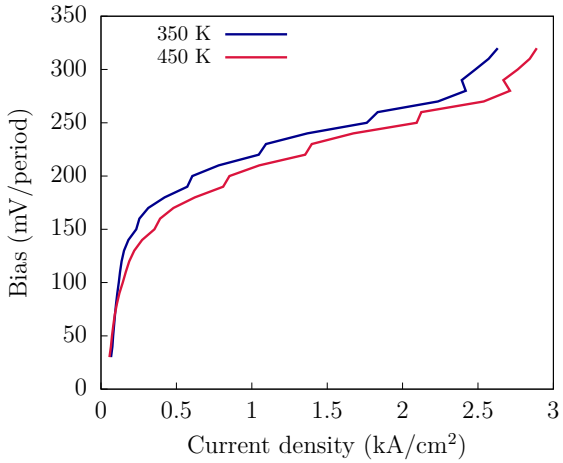

(a) Simulated I-V curve.

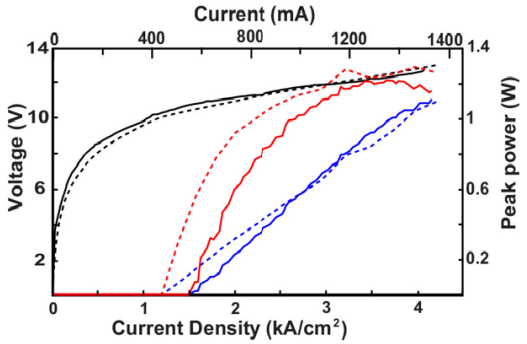

(b) Experimental I-V curve.

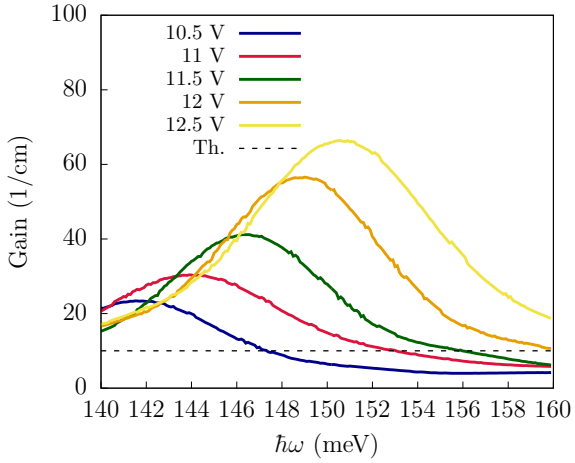

(c) Simulated gain spectra.

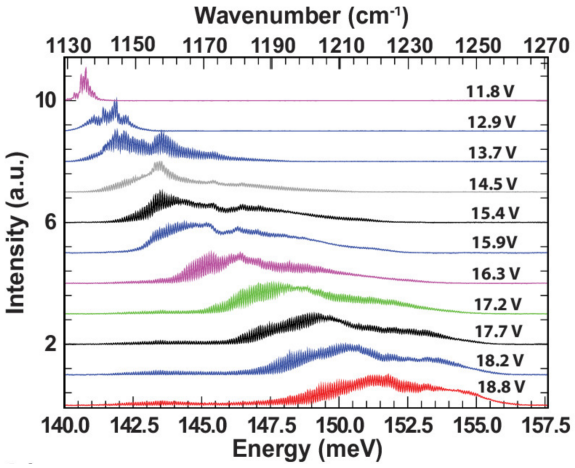

(d) Experimental gain spectra.

Figure 4.7: Data for Bismuto *et al.*'s mid-IR QCL [52]. (a) Simulated I-V curve for $T_{\text{simulation}} = 350$ and 450 K. (b) Experimental I-V curve of the device at $T_{\text{Heatsink}} = 300$ K. The design was reported to emit at ∼8.5 μm and exhibit large tunability of 100 cm^{-1}. (c) Simulated gain spectra for different applied biases (10.5 V to 12.5 V) at $T_{\text{Simulation}} = 350$ K. The gain threshold for the device is established at $g_{TH} = 10$ cm^{-1}. (d) Experimental gain spectra for the same device, which aims to show the experimentally observed Stark shift of the gain peak at $T_{\text{Heatsink}} = 300$ K. The experimental plots where taken from [52].

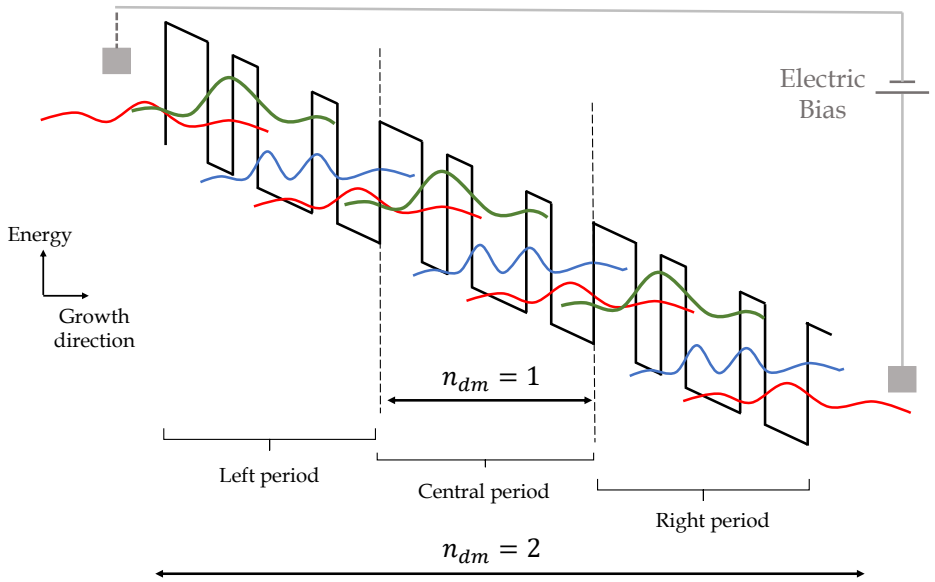

Figure 4.8: Schematic representation of the QCL active region and basic modules, where the central and neighbouring (left and right) periods are shown. The parameter n_{dm} controls the number of periods included in the central region of simulation. For $n_{dm} = 1$, a single period is included. For $n_{dm} = 2$, the neighbouring left and right periods are also included within the central period for the computation of $\hat{\rho}$.

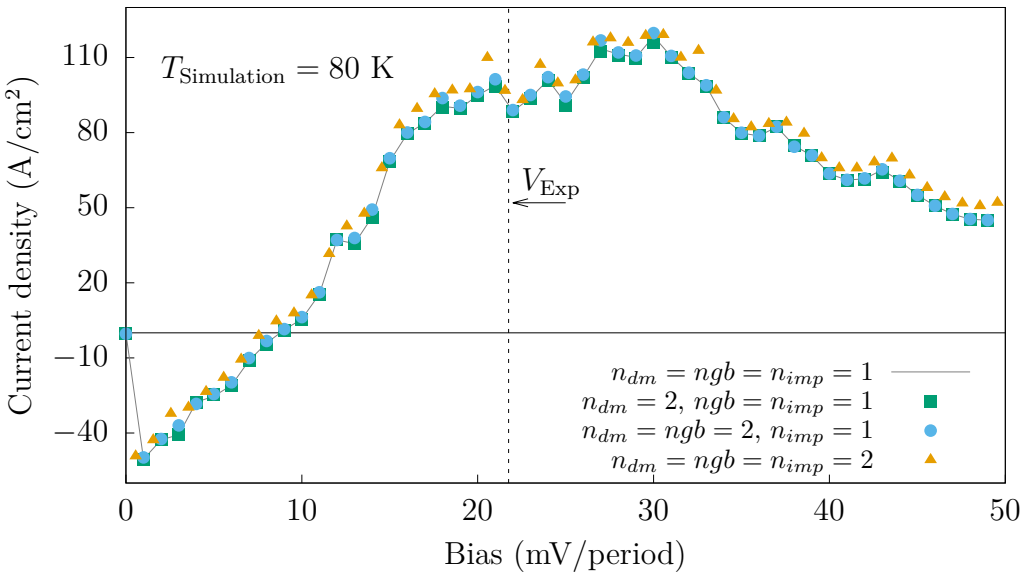

Figure 4.9: I-V plot for Mahler *et al.*'s THz-QCL [49] for $T_{\text{Simulation}} = 80$ K. Several simulations for a varying number of neighbours (ngb and n_{imp}) and periods (n_{dm}) are shown. The vertical dashed line indicates the design bias of the structure, 21 mV/period.

4.2.3 Negative current densities

The I-V curve in Fig. 4.1 (a) shows a remarkable feature: negative current densities. This problem was already addressed in [26], the paper in which the PERLind approach is presented. Moreover, Kiršanskas *et al.* in [26] point out that the PERLind approach can provide non-zero currents for a zero applied bias, a feature we have also observed in our simulations. Negative current density values in the I-V curve could be originated from two factors: either they naturally arise within the PERLind approach, signalling a limitation of the transport model, or they are related to the choice of boundary conditions for the computation of $\hat{\rho}$. As we have already discussed, we limit the simulations to a finite number of periods known as the *central region*, given by n_{dm} (see Fig. 4.8) and we impose periodic boundary conditions to compute $\hat{\rho}$.

We can test if the I-V curves remain invariant when incorporating more periods to the central region. Figure 4.9 shows the results of several simulations with increasing number of n_{dm} and neighbours ngb and n_{imp} for Mahler *et al.*'s device, where ngb controls the distance up to which the phonon scattering matrix elements are evaluated (i.e. $ngb = 1 \rightarrow$ first neighbours) and n_{imp} does the same for impurity scattering. As shown in the figure, the I-V plot remains fairly invariant for the different n_{dm}, ngb and n_{imp} values chosen. The I-V curve exhibits negative values below 10 mV/period for all the simulations. The transition from negative to positive J occurs at the same bias point except when $n_{dm} = ngb = n_{imp} = 2$ is taken. Here, the region of negative current is 1 mV/period smaller; the transition to positive values takes place at 7 mV/period instead of 8 mV/period. These results support the conclusion that negative currents are most likely linked to the model and not to the LQCL computation package or boundary conditions. Unphysical negative currents can naturally arise within the PERLind approach. Nevertheless, the results in Fig. 4.9 also prove the robustness of the LQCL package in providing roughly the same curve, regardless of the level of accuracy of the simulation (i.e. adding more neighbours to the computation).

4.2.4 The optical AC field

The LQCL package enables the simulation of laser ignition by applying a non-zero AC field to the structure, as given in eq. (3.12). In Fig. 4.10 (a) we observe that the oscillating optical field yields an increase in current density at the bias point at which it is turned on, as expected (see discussion on laser observables in 3.3). In Fig. 4.10 (b) we see the effect of the AC field on gain. We have already discussed that an oscillating AC field reduces population inversion and consequently, gain. As the intensity of the optical field increases, gain decreases approaching zero, where the transparency condition is reached. When $g = 0$, population inversion is completely lost and the field has redistributed carriers equally between the ULS and LLS. Surprisingly, our results in plot (b) show that gain takes negative values instead of saturating at zero. This might be indication of further transitions to higher levels or absorption mechanisms in the structure.

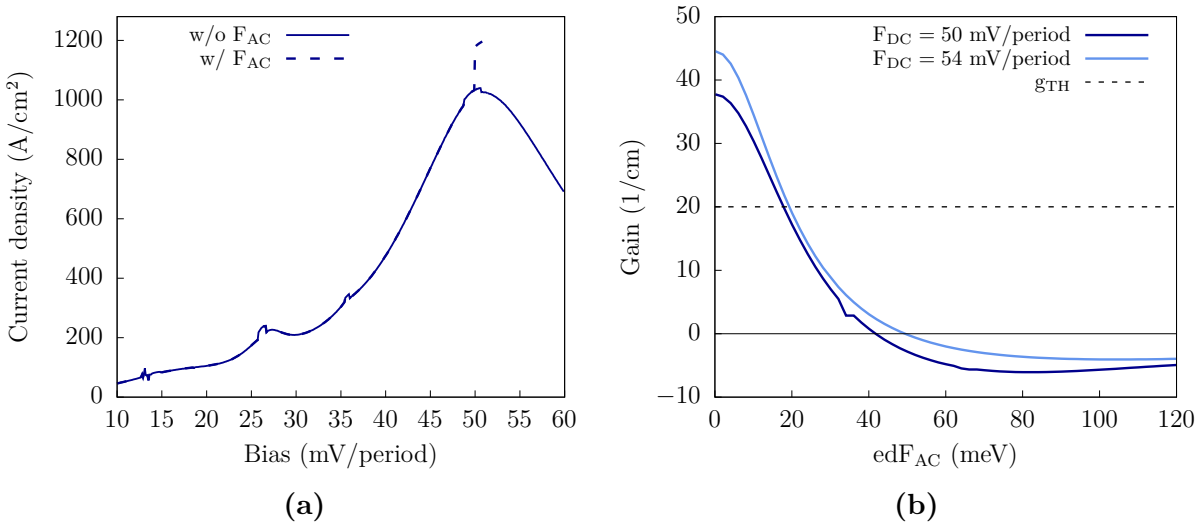

Figure 4.10: Data for Li *et al.*'s THz-QCL [50]. (a) Simulated I-V curve of the QCL. The optical AC field is turned on at 50 mV/period (dashed line), which yields an increase in current. (b) Laser gain versus optical AC field for two fixed DC biases: 50 mV/period (dark blue) and 54 mV/period (light blue). The gain threshold (horizontal dashed line) is established at $g_{TH} = 20$ cm^{-1}.

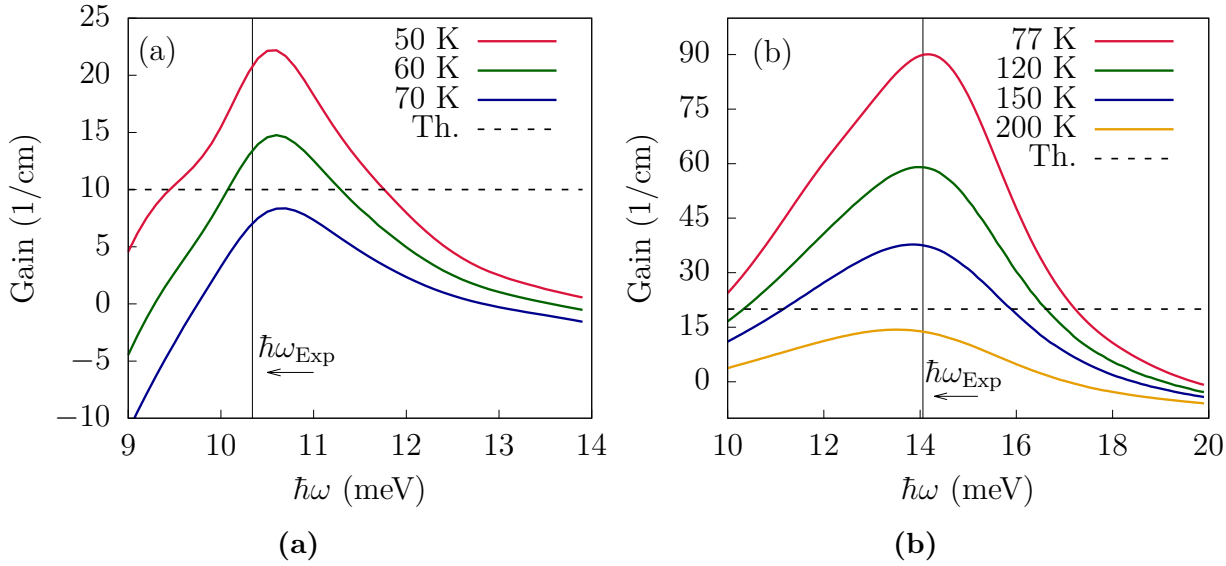

Figure 4.11: Gain spectra for devices in [49] (a) and [50] (b). (a) Data was gathered at 21 mV/period. The design bias of the device is 1.6 kV/cm ($\sim$ 21.76 mV/period). It lases at $\nu_{\text{Exp}} =$ 2.5 THz and it experimentally exhibited a maximum operating temperature of $T^{\text{max}}_{\text{Heatsink}} = 58$ K [49]. The threshold is established at 10 cm^{-1}. For the simulation of this device, 10 WS states were required. (b) Data obtained at 50 mV/period, the desing bias of the QCL. It lases at $\nu_{\text{Exp}} = 3.4$ THz until $T^{\text{max}}_{\text{Heatsink}} = 123$ K [50]. The threshold is established at 20 cm^{-1}.

4.3 Gain spectrum and emission frequencies

As we have already shown in Figs. 4.1 (c) and 4.7 (c) the LQCL package predicts the gain spectrum of a QCL at a chosen bias point, when the optical field (3.12) is non-zero. Our results report gain above threshold g_{TH}, which shows we can simulate laser operation. We have only considered gain at Positive Differential Resistivity (PDR) regions, as there are stability and domain formation problems linked to NDR regions [55, 56]. Further examples of the simulated gain spectra are shown in Fig. 4.11. In Fig. 4.11 (a), the curve peaks between 10 and 11 meV. This is coincident with the experimental lasing frequency of 2.5 THz (∼10.34 meV). The simulations show gain for temperatures below $T^{\max}_{\text{Simulation}} = 60$ K, while the device was reported to operate to $T^{\max}_{\text{Heatsink}} = 58$ K [49]. This is consistent with our results, although we expected to see a large shift between $T_{\text{Simulation}}$ and T_{Heatsink} as this device was operated in cw[2]. The results for Fig. 4.11 (b) are also consistent with experimental data: a maximum of $T^{\max}_{\text{Heatsink}} = 123$ K was reported and no gain is observed below $T_{\text{Simulation}} = 150$ K, yielding an expected shift of 30-60 K between $T_{\text{Simulation}}$ and T_{Heatsink} in pulsed mode operation.

QCLs are tunable devices: the peak of the gain spectrum can shift to higher frequencies with increasing bias. This is known as the Stark shift of the gain peak, which LQCL is able to reproduce, as it is shown for a mid-IR QCL in Fig. 4.7 (c). This effect is easier to observe in IR-QCLs simulations as the voltage drop along IR-QCL structures is larger than in THz-QCLs. IR-QCLs require larger applied biases to operate and to pump electrons into the states, which explains why the Stark effect is more significant for these devices.

4.4 The simulation temperature

There is a single temperature parameter for both electronic, T_E, and lattice, T_L, temperatures within LQCL: the same value is used for the temperature of electrons in the subbands and the Bose-Einstein LO-phonon distribution. However, carriers are usually hotter than the lattice and the $T_E \approx T_L$ approximation does not always hold [57]. Furthermore, it has been long debated whether electrons are thermalized or not in the subbands [27, 58]. This points out the inaccuracy of assuming a single electronic temperature for all subbands and emphasizes the complexity of a rigorous treatment of temperature. Some authors assume a temperature difference of 70 K to 100 K between electrons and LO-phonons [27]. Nevertheless, such difference depends on the power carried by the particles, the lattice temperature and active region design. We can check how T_E depends on these parameters by using our group's NEGFs code for QCL simulation [25], where the subband electronic temperature is self-consistently computed for constant T_L at fixed bias. NEGFs provide the occupation function $f^i_{\boldsymbol{k}}$ of each subband i at a given operation point. The electronic temperature of the i-th subband can then be inferred by fitting the occupation function to an exponential Boltzmann-type of distribution [27], $f^i_{\boldsymbol{k}} \propto e^{-E_{\boldsymbol{k}}/k_B T^i_E}$. The results of the NEGFs simulations for six different devices are shown in Table 4.2. In the table, we show

[2] At cw operation, the lattice cannot relax and cool down while the electric field is applied to the structure. Hence, $T_L \gg T_{\text{Heatsink}}$ in this case. $T_L \approx T_{\text{Heatsink}}$ is more likely to hold for pulsed mode operation, where the lattice can relax between pulses. Nevertheless, it is also expected to have $T_{\text{Simulation}} > T_{\text{Heatsink}}$ even for pulsed mode.

the power per particle carried by electrons for a given V bias point,

$$P_p = \frac{V \times J}{n_{2D}}, \tag{4.1}$$

where n_{2D} is sheet electron density. The value of V was taken close to the design bias of the device. It is important to note that the electronic temperatures in Table 4.2, T_E^{avg}, are the average of the individual subband temperatures at the operation point. These individual subband temperatures are explicitly shown in Table 4.3 for the device in [50] at two different biases.

The *excess temperature*,

$$\Delta T^i = T^i_{ex}(T_L) = T^i_E - T_L, \tag{4.2}$$

introduced by Albo and Flores in [57] measures the deviation of the electronic temperature T^i_E from T_L. In our considerations, we drop the subband superscript and use, as above mentioned, an averaged T_E to compute ΔT. A non-zero excess temperature indicates that $T_E \neq T_L$ and points out the need to input T_E and T_L individually within the LQCL simulation package. Therefore, we have separated the contribution of electronic T_E from the lattice T_L in LQCL and tested the effect of a higher T_E ($T_E > T_L$) in the simulations. We have repeated the I-V curves using the averaged subband electronic temperature T_E^{avg} provided by the NEGFs (see data in Table 4.2). Both T_E and T_L have been kept constant throughout the new simulations.

We have observed that using $T_E \neq T_L$ can help increase the current density in the high bias region. This is specially significant for those THz-QCLs for which the excess temperature is large ($\Delta T > 80$ K), such as Han *et al.*'s device. As an example, we show the simulations for this THz-QCL in Fig. 4.12, where three simulations are compared: an LQCL simulation with a single temperature parameter ($T_E = T_L$), a NEGFs simulation, and a second LQCL simulation with two temperature parameters ($T_E \neq T_L$, where the value for T_E was taken from Table 4.2 for the corresponding device). The results in Fig. 4.12 show that at low biases (< 30 mV/period) the current density is relatively independent of the choice for electronic temperature. It is safe then to assume that $T_E \approx T_L$ in this region, as we did for the preliminary simulations in section 4.1. However, at high biases (> 30 mV/period), the curves show that current density increases for $T_E > T_L$; the LQCL simulations come closer to both NEGFs and the experimental data. We must note here that these simulations were run for first neighbours. The use of $T_E \neq T_L$ has a less significant effect in high-temperature devices like the mid-IR in [52] or the high-temperature THz-QCL in [16]. Therefore, these results show that although a more accurate modeling of temperature is required, we cannot attribute LQCL's current underestimation solely to the way temperature is considered in the package.

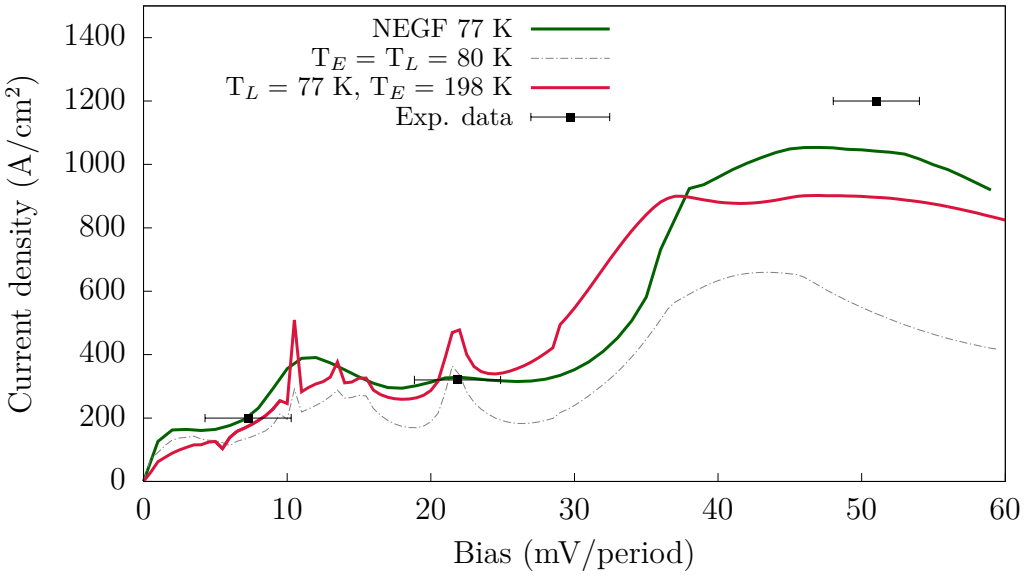

Figure 4.12: I-V plot for Han *et al.*'s D2 device in [17] for different temperatures and simulation methods (NEGFs and LQCL). The dotted grey line corresponds to the LQCL simulation with $T_E = T_L = 80$K. The green solid line is the NEGFs simulation with $T_L = 77$ K. The red solid line is the LQCL simulation with $T_L = 77$ K and $T_E = 198$ K, where this electronic temperature value was computed from the NEGFs simulations (see Table 4.2).

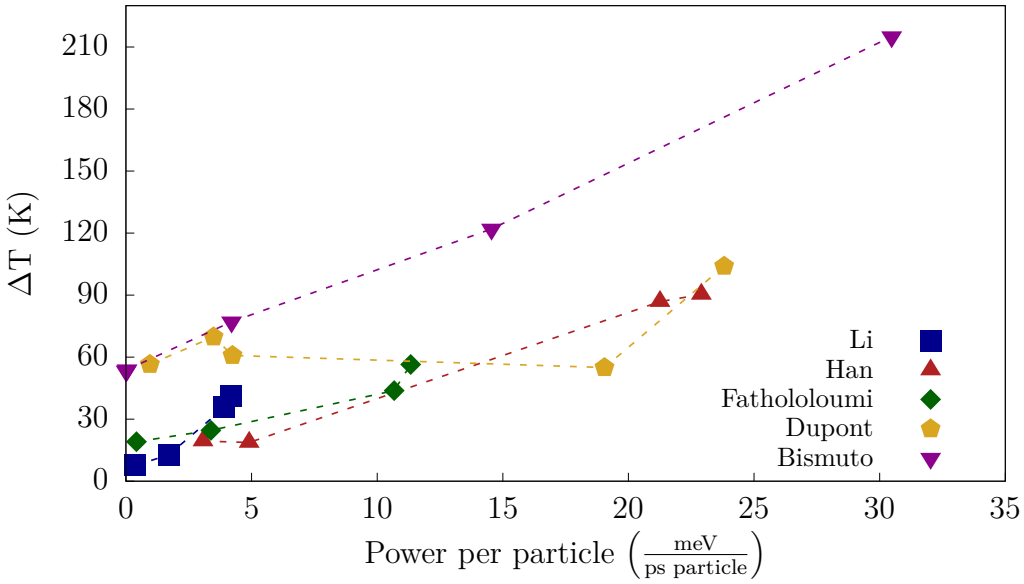

Figure 4.13: Excess temperature ΔT as a function of the power dissipated per particle, for the QCL devices in references [16, 50, 22, 17, 52]. Data was produced using NEGFs simulations. The excess temperature was obtained by fitting the electronic subband occupations from NEGFs to an exponential Boltzmann-type of distribution function, e^{-E/k_BT} and averaging over the individual temperatures of the subbands.

Table 4.2: The average electronic subband temperatures T_E computed through NEGFs simulations for a fixed lattice temperature T_L and an applied bias per period. The results shown correspond to six QCL devices [16, 17, 22, 38, 50, 52].

Device	Power (nW/particle)	T_L (K)	T_E^{avg} (K)	$T_E - T_L$ (K)
Li *et al.* [50]	0.8	150	186	36
Han *et al.* [17]	2.0	77	157	80
Fathololoumi *et al.* [16]	1.8	200	245	45
Williams *et al.* [16]	1.4	77	220	143
Dupont *et al.* [22]	3.8	140	240	100
Bismuto *et al.* [52]	5.9	300	475	175

Table 4.3: Individual electronic temperatures T_E for each of the five WS subbands for the THz-QCL in [50], computed through NEGFs simulations. The fixed lattice temperature is $T_L = 150$ K. The results are shown for two different operation points, at 16 mV/period (Table 4.3) and 47 mV/period (Table 4.4).

Table 4.4: 16 mV/period

Subband	T_E (K)
1	170.5
2	152.8
3	152.2
4	168.7
5	164.5

Table 4.5: 47 mV/period

Subband	T_E (K)
1	183.4
2	160.1
3	201.1
4	209.8
5	173.7

4.5 Impact of heat dissipation

The LQCL simulation package does not consider lattice heating effects; that is, *thermal feedback* is not included [27]. Nevertheless, the range of excess temperatures in Table 4.2 and the disagreement between simulation and experiment at high applied bias seem to suggest that energy dissipation has a prominent role in transport phenomena and can affect the current density flowing in the device. The excess temperature, and in particular, the evolution of T_E with the applied bias serve as tools to model lattice heating in our simulations. These parameters can be used to justify the discrepancy between our simulations and the experimental data.

We will try to quantify the heating of the lattice through two parameters: the excess temperature, ΔT, and the power per particle, P_p (4.1). As we have already detailed, ΔT measures the heating of the charge carriers with respect to the lattice, which is assumed to be kept at constant T_L. The power per particle has its origin in the electric field applied to the QCL structure. Electrons moving in an electric field carry a net power transferred by the field. This is given by eq. (4.1) which constitutes the power that electrons can transfer to the lattice through scattering mechanisms. Such power is dissipated by heating the lattice, i.e. activating LO-phonons. Therefore, there must exist a correlation between ΔT and P_p: the higher the power carriers need to dissipate, the larger the excess temperature will be. This correlation is shown in Fig. 4.13, where NEGFs were used to obtain the data.

We observe that the correlation between the dissipated power and the excess temperature is almost linear for most devices. The exception is Dupont *et al.*'s QCL [22], which shows little temperature dependence to the heating. Fig. 4.13 also shows that the excess temperature ranges from 10 K to 100 K for the THz-QCL devices in the figure, while it goes from 60 K to almost 220 K for the only mid-IR QCL in the figure. The results confirm that T_E, which can be inferred from ΔT, is a dynamic variable that changes with the bias. A similar conclusion was presented by Harrison *et al.* in [31]. Here, authors propose a linear relation between T_E and T_L dependent on the current density,

$$T_E = T_L + \alpha_{e-l} J \tag{4.3}$$

to model subband temperatures in QCLs. In [31], authors find the coupling constant α_{e-l} to be α = 7.6-6.1 K/(kA cm^{-2}) for IR-QCLs and $\alpha \approx$ 47 K/(kA cm^{-2}) for THz-QCLs. We have used this relation to model T_E within LQCL with little impact on our curves.

4.6 The electronic temperature

The arguments in the sections above show that a careful choice of the electronic temperature can increase the current density. Moreover, the analysis of the heating effects in the device points out the inaccuracy of considering T_E constant throughout the simulations. Therefore, in this section we aim to find a relation between the carrier heating and the electronic temperature which would allow us to self-consistently input T_E in the LQCL package for each operation point.

4.6.1 A simple model to compute T_E within LQCL

As previously discussed, the electronic temperature T_E can be inferred from the state occupation density, by fitting the individual subband occupations to a Boltzmann distribution function (see [27] for a detailed example of this fit). This kind of approach requires in-plane resolution, which we lack in PERLind and LQCL. Alternatively, our suggestion is to compute T_E focusing on the energy stored by the lattice. Approaches like this have already been attempted in Harrison *et al.*'s aforementioned paper [31], where authors use a *kinetic energy balance* method to compute an averaged subband T_E. Our proposal is that the power dissipated by electrons will be invested in varying the number of phonons in the lattice.

The relaxation of electrons and consequent activation of phonons can be accounted for through the following energy balance equation:

$$V \times J = \hbar\omega_{LO} \sum_{\alpha,\beta} n_\alpha \Big(R^{EM}_{\alpha\to\beta}(T_E, T_L) - R^{ABS}_{\alpha\to\beta}(T_E, T_L) \Big). \tag{4.4}$$

Here, $V \times J$ is the net power that the external field transfers to electrons per unit period and surface area; n_α is the electron sheet occupation density of state α; $R_{\alpha\to\beta}$ corresponds to the scattering rates for the emission (EM) or absorption (ABS) of a LO-phonon (see in Appendix A for the explicit expressions). As argued in section 2.1.1, we assume that LO-phonons are the dominant phonon type in the QCL structure. The sum in α and β is extended to all quantized states in one period. Terms with $\alpha \neq \beta$ are intersubband transitions, while $\alpha = \beta$ correspond to intrasubband thermalization. The Left Hand Side

(LHS) of eq. (4.4) accounts for the power transferred from the field to the charged carriers. The Righ Hand Side (RHS) of (4.4) gives the total energy stored by the lattice in LO-phonons. The numerical resolution of eq. (4.4) for a given operation point provides the T_E that balances the electron-phonon energy transfer.

The colourmap in Fig. 4.14 shows the function

$$f(V, T_E) = \text{LHS} - \text{RHS}, \tag{4.5}$$

where LHS and RHS are those in eq. (4.4). Positive values correspond to LHS > RHS, indicating an excess of power carried by the electrons that the lattice cannot get rid of in the form of phonons. Negative values are LHS < RHS, where the lattice has stored more energy than that transferred by the electrons. A blue contour line marks the values for which LHS = RHS, signalling the T_E values we are interested in inputting in LQCL.

The results in Fig. 4.14 for Fathololoumi et *al.*'s device show that at low applied bias (<20 mV/period), it is correct to assume $T_E \approx T_L$, as physically expected. As the bias increases, the T_E value that satisfies (4.4) deviates from the lattice temperature, $T_E > T_L$. The results in the figure point out that the excess temperature can vary from ΔT = 20 K in the low bias region to ΔT = 120 K at higher biases, which is larger than the ΔT^{max} = 60 K we had predicted in Fig. 4.13 for this THz-QCL [16]. The peak observed at 25 mV/period is most likely associated to a computational issue rather than the activation of a scattering mechanism. In figure 4.15, we present the results for the I-V curve of the same device by self-consistently inputting T_E according to (4.4). We compare these results with our group's implementation of NEGFs and the LQCL package assuming constant $T_E = T_L$. As it can be seen in the figure, the LQCL simulation with the self-consistent T_E does not significantly improve the LQCL simulation with $T_E = T_L$. If we compare the LQCL results with the NEGFs data, we observe that the simulations deviate from each other when $T_E > T_L$ in the colourmap. By looking at Fig. 4.14, we see that T_E approximately grows from 200 K to 300 K from biases 25 mV/period to 39 mV/period. In the same bias region, the results in Fig. 4.15 show that the LQCL curve is below the NEGFs current density values. The same situation repeats from 40 mV/period to 52 mV/period, where assuming $T_E = T_L$ translates again in LQCL underestimating the current density with respect to the results from NEGFs.

4.6.2 Limitations of the LQCL package to model T_E

In order to self-consistently compute the subband electronic temperature, more advanced simulation methods turn, for instance, to Boltzmann transport theory or heat diffusion equations [59, 60]. The increased complexity of such methods yields an accordingly larger computation time. Since PERLind's, and consequently LQCL's, major asset is its computational speed, it is not worth sacrificing the lightness of the approach for a more rigorous treatment of temperatures with microscopic theories. Lightness is PERLind's main advantage with respect to more robust methods like NEGFs [25]. Thus, any attempts to improve the LQCL package should keep the computation time low. This reasoning stands behind the simple model to compute T_E proposed in section 4.6.1.

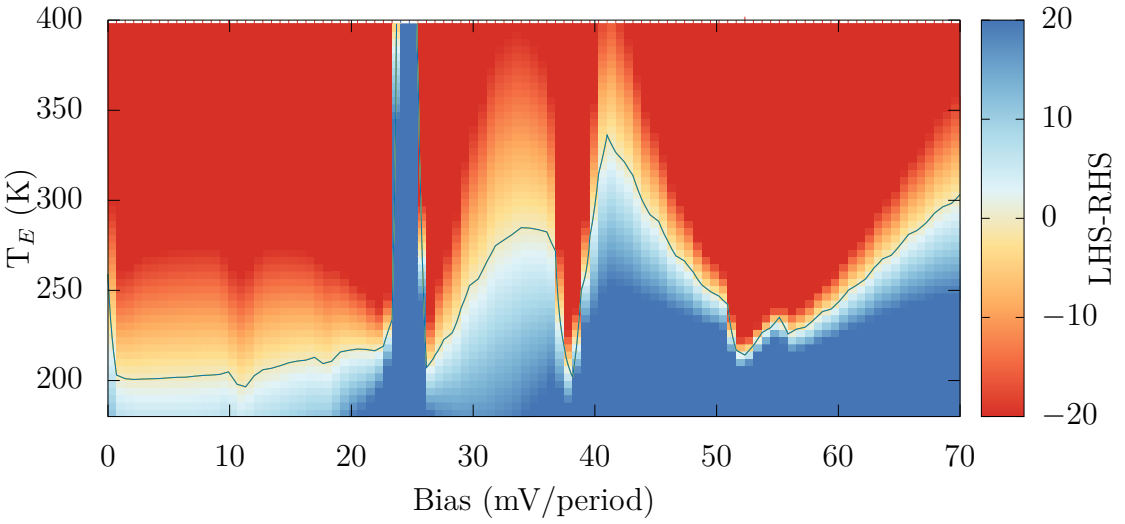

Figure 4.14: Heat map that shows the energy balance equation given in eq. (4.4), as a function of the electronic temperature T_E and the applied bias per period for the THz-QCL in [16]. The lattice temperature was fixed to $T_L = 200$ K. The colour bar shows the difference between the Left Hand Side (LHS) and Right Hand Side (RHS) of eq. (4.4). Positive values show that LHS > RHS, while negative values correspond to LHS < RHS. The solid blue line indicates the contour line corresponding to LHS = RHS, the temperature and bias values at which energy balance is achieved.

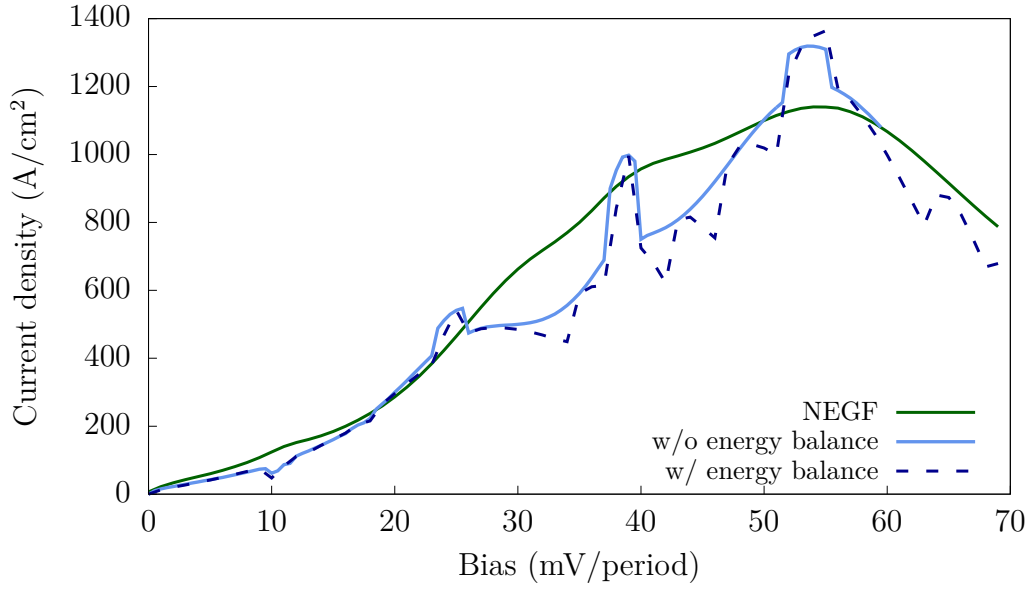

Figure 4.15: I-V plot for Fathololoumi *et al.*'s THz-QCL [16] for $T_L = 200$ K. The NEGF simulation is shown in green. The simulations with LQCL are shown in blue: one with $T_E = T_L = 200$ K (w/o energy balance, solid light blue) and one with $T_L = 200$ K where T_E is computed according to the energy balance equation (4.4) (w/ energy balance, dashed dark blue).

There are a few simplifications within the LQCL package that limit a rigorous modeling of the electronic subband temperature. The main one is that the density matrix computed with the PERLind approach is not k-resolved. Thus, the LQCL package must assume that all electronic subbands have the same temperature. In reality, each subband i has an individual T_E^i that depends on the bias and lattice temperature, as discussed in Table 4.3 [61, 62]. A single T_E for all subbands implies that electrons instantly thermalize. Using a 3D density matrix approach, Burnett *et al.* have shown that the electronic subband distributions are highly non-thermal [27]. In the PERLind approach, we assume a thermal distribution for the lateral electron degrees of freedom to construct the Lindblad coupling tensor (3.5) (see Appendixes A, B and C). Therefore, immediate thermalization is intrinsic to the formalism upon which the LQCL simulation package is developed. We must also point out that the sum in (4.4) is extended to number of energy levels per period of our choice, usually limited to the bound well levels relevant for transport and the photoemissions. As we have argued before, the continuum is usually ignored in the simulations. Ideally, the summation in (4.4) should cover all the WS energy levels in the period, including the continuum. This also restricts the accuracy of our implementation of eq. (4.4) in LQCL.

4.7 Implementation of IFR scattering in LQCL

In this section, we present the results obtained after including IFR scattering in the LQCL package. The implementation of this scattering mechanism was done following the calculations summarized in Appendix C, according to the PERLind approach. Here it is important to remark that the definition of the jump operators $L_{\alpha,\beta}$ for the construction of the Lindblad dissipator (3.9) within the PERLind approach is not unique. In fact, different choices of operators might describe different physics [26]. This is particularly important for IFR scattering because depending on our operator choice, we can establish a correlation between the fluctuations at different interfaces. For our implementation of IFR in LQCL we have assigned an individual jump operator to each interface; that is, we don't allow for correlations of the fluctuations at each interface since this is unlikely to occur during the growth process of the sample [34]. The correlation functions to model the shape of the interface profile and fit parameters Δ and Λ that we have used for our simulations have been taken from [34]. These are similar to the parameters usually found in literature [27].

The inclusion of IFR improves quantitatively the results of the LQCL simulations by increasing the current density. This can be seen in Fig. 4.16 (a), where results for Dupont *et al.*'s device with and without IFR scattering are compared. In the figure, we observe that including IFR raises J and changes the curvature of the I-V plot above the shoulder at 16 mV/period. It also yields a flatter NDR region, closer to what experimentally is observed. In Fig. 4.16 (b), we show the increase of J_{TH} when IFR is added. The results that include IFR scattering in Fig. 4.16 (b) seem to follow an exponential trend before plateauing at higher temperatures. The temperature shift between the experimental data and the LQCL simulation with IFR scattering agrees well with the stable excess temperature of $\Delta T = 60$ K found in Fig. 4.14 for this THz-QCL [22].

The effect of IFR scattering is expected to be larger in IR-QCLs as the scattering matrix element is proportional to the CB offset, typically larger in IR-QCLs (see Appendix C). In Fig. 4.17, we present the simulation results for Bismuto *et al.*'s IR-QCL. In the plot, we see that IFR scattering extends the I-V curve to 4 kA/cm^2, which perfectly agrees with the $J^{\max} = 4$ kA/cm^2 reported experimentally (see Fig. 4.7). This $J^{\max}$ value could not be reached before, without adding IFR. However, it must be pointed out that by adding IFR, we also observe an unphysical negative current density at low applied bias, a feature that had not appeared before for this device.

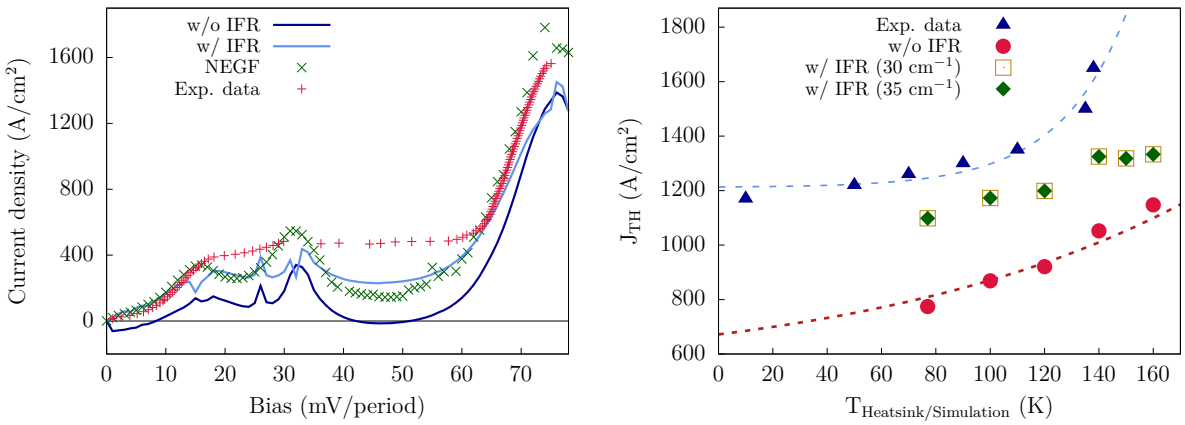

Figure 4.16: Data for Dupont *et al.*'s THz-QCL [22] (a) I-V curve for $T_{\text{Simulation}} = 77$ K, with (w/, light blue) and without (w/o, dark blue) IFR scattering. IFR is modelled through an exponential correlation function (2.7), with $\Delta = 10$ nm and $\Lambda = 0.2$ nm. Experimental data is shown with red crosses. Results from our group's NEGFs code are shown in green. (b) Experimental and simulated data with (w/) and without (w/o) IFR scattering for J_{TH} as a function of temperature for the same device. g_{TH} is $g = 30$ cm^{-1} (red dots and gold boxes) and $g = 35$ cm^{-1} (green diamond). T_{Heatsink} corresponds to the experimental values and $T_{\text{Simulation}}$ for the simulations. The fit functions are $J_{TH} = J_0 e^{T/T_0}$, where $T_0 = 30$ K for the experimental data and $T_0 = 110$ K for LQCL.

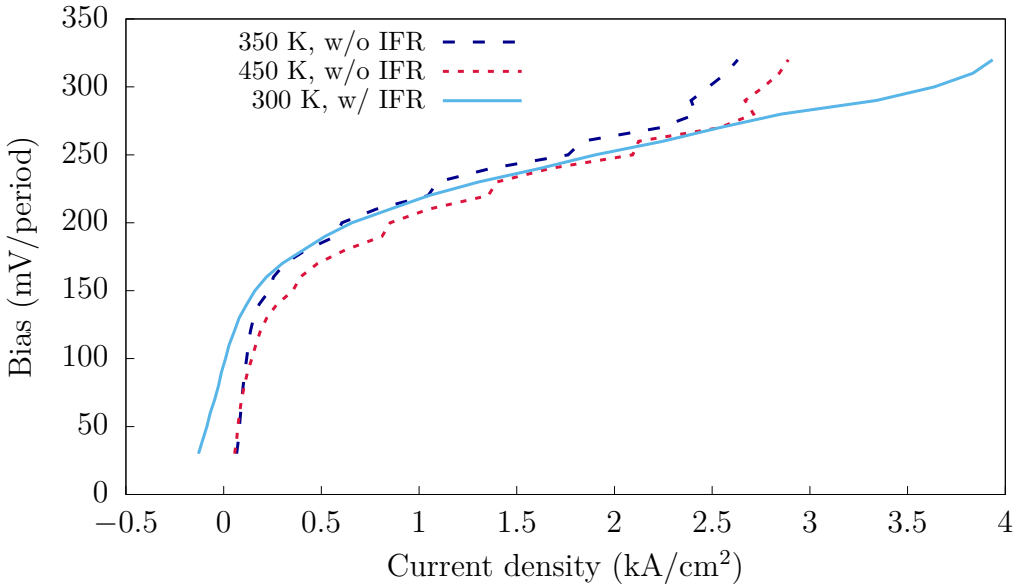

Figure 4.17: I-V curve for Bismuto *et al.*'s mid-IR QCL [52] without (w/o, dashed lines) and with (w, solid line) IFR scattering. Simulations are run at $T_{\text{Simulation}} = 300$ (w/ IFR), 350 and 450 (w/o IFR). We observe that adding IFR scattering increases J_{max} from 3 kA/cm^2 to 4 kA/cm^2, as observed experimentally.

Chapter 5 | Numerics

The main asset of the PERLind approach is its computational lightness. As discussed in section 2.2.3, its speed stems from the lack of in-plane resolution; that is, the density matrix we compute is not k-resolved. Therefore, state populations are known, but we do not have access to the subband electronic distributions. While this sacrifices the accuracy of the simulations, LQCL manages to qualitatively (and to a certain extent, quantitatively) reproduce transport in QCLs. In this chapter, we discuss the computation times associated to the LQCL package. It must be noted that, unless otherwise stated, the computation times we show here correspond to simulations to first neighbours.

5.1 Computation time for LQCL

The CPU models on which the simulations in this thesis have been run are Intel® Core™ i7-8700 3.2 GHz (Mass181 and Mass182) and Intel® Core™ i7-7700 3.60 GHz (Gluon and Myon). The *user* time as a function of the number of WS states is shown in Fig. 5.1. Here, user time is taken as the CPU time needed to execute the process[1]. It is is different from wall clock time, which is the total time between the process is called and finished. User time does not take into account that the CPU can be running other processes simultaneously. Nevertheless, the times in Fig. 5.1 are approximately equal to the corresponding wall clock times we would measure with our wrist watch because the simulations were run individually in single cores.

The results show that the computation time for a single I-V point (Fig. 5.1, a) is below 10 minutes for simulations with 5 WS states or less. This is the case for most THz-QCL designs [16, 17, 50]. Active region designs based on *minibands* (i.e. subbands that are very closely spaced) or mid-IR devices require more WS states in their simulations (over 8 WS states) [49, 52, 53]. In such cases, user time increases to 20-35 minutes, depending on the number of momentum points used to construct the scattering matrix elements. If the gain spectrum is included in the simulation (see Fig. 5.1, b), the computation time rises to 16 minutes for 5 WS states, and to 25-55 minutes for 10 WS states.

The number of momentum points chosen determines how many points will be used to compute the scattering integrals. The bottleneck of the simulations is precisely these numerical integrals. The implementation of IFR scattering in the LQCL package, which requires less integrals than the rest of the mechanisms (see approximation in (C.3)), yields an increase in user time below 30 seconds per data point (see Fig 5.4). On the contrary, impurity scattering is the heaviest of the three scattering mechanisms, as there is one overlap integral associated to each impurity. In Fig. 5.2, we show that the computation time approximately increases as $t \propto N^3$, where N is the number of neighbours.

[1]The total CPU time to run the process is a sum of user and *system* time, where system time corresponds to the time spent in a priviledged mode within the kernel of the CPU. In our simulations, system time is negligible in comparison to user time.

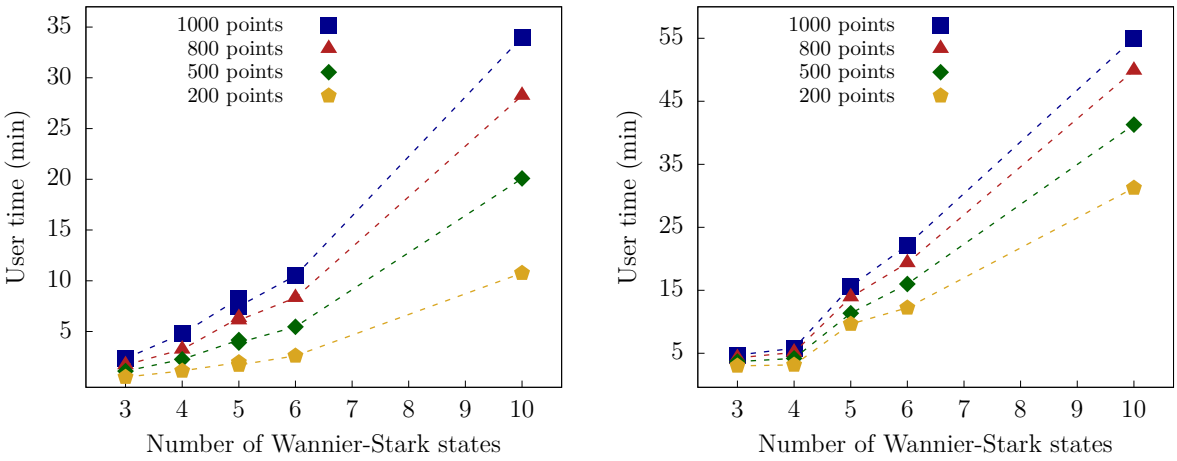

(a) Without gain. **(b)** With gain.

Figure 5.1: User time for LQCL simulations as a function of the number of WS states required by the device simulated. No IFR scattering was considered. (a) Only a single I-V point is computed. (b) One I-V point and 11 gain points are computed. The simulated devices are [17] (3 states), [16] (4 states), [22] and [50] (5 states), [38] (6 states) and [49] (10 states). The effect of choosing a different number of points (1000, 800, 500 or 200) for the discretization transverse and longitudinal momenta is shown.

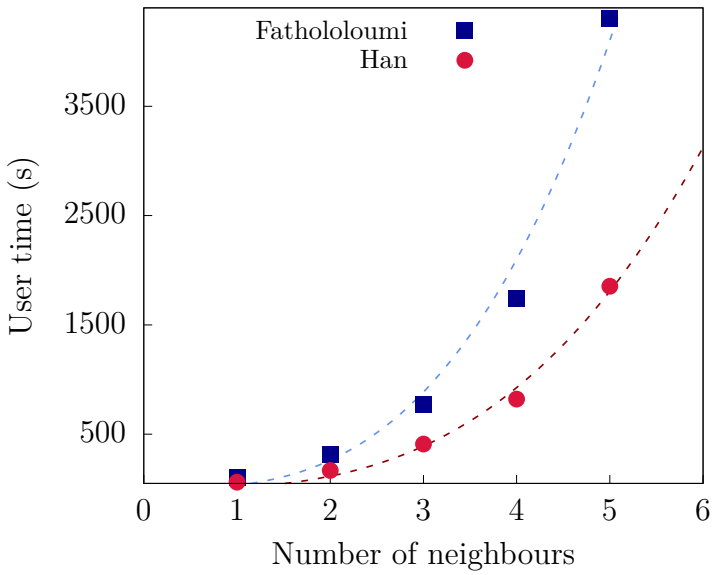

Figure 5.2: User time as a function of the number of neighbours (first neighbours (1), second neighbours (2) and so on) for Fathololoumi *et al.*'s THz-QCL (blue square) [16] and Han *et al.*'s THz-QCL [17]. The fit function corresponds to $f(x) = Ax^3$, where $A = (32.8 \pm 1.5)$ (blue dashed line) and $A = 14.5 \pm 0.5$ (red dashed line).

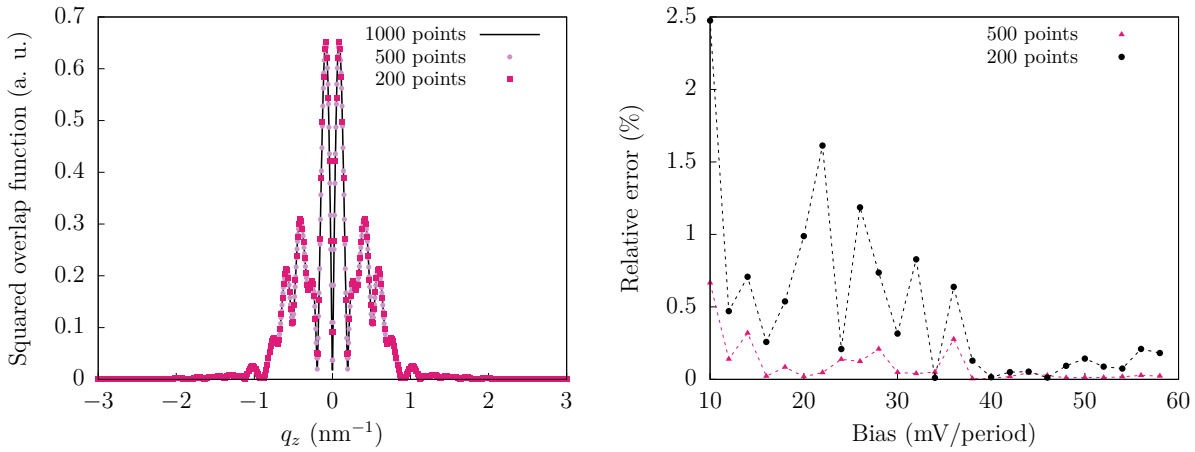

(a) **(b)**

Figure 5.3: (a) LO-phonon scattering integral of two states in the central period of the device in [50], for different momenta discretizations. (b) Relative error of the current density for Li *et al.*'s THz-QCL [50] as a function of the applied bias. We compare the results for 1000 momentum points (the *default* discretization) with 500 and 200 points.

The LQCL package first builds the Lindblad dissipator for LO-phonons, impurities and IFR. Then, it computes $\hat{\rho}$. With $\hat{\rho}$, we can obtain the current density for a given bias point. To compute the gain spectrum, the time-varying AC field must be included. As it can be seen in the bar plots in Fig. 5.4, the simulation of the gain spectrum is independent of the number of points for longitudinal and transverse momenta: the corresponding Lindblad dissipator, with all its numerical integrals, has already been constructed in a previous step. This has a very important consequence: LQCL computes gain spectra without any additional computational cost once the I-V curve has been obtained.

The default number of points used for the scattering integrals is 1000. It has been found that such number can be reduced without compromising the accuracy of the results. The computation time per data point is roughly halved with a reduction of 50% in the number of momenta points for the scattering integrals. The relative error is below 1% for the I-V curves when 500 points are used for the integrals (see Fig. 5.3).

5.2 Comparison with NEGFs

The use of NEGFs for QCL simulations is a well-established and robust method to simulate quantum transport in QCLs [10, 12]. Its major drawback is its large computation load. Our group's implementation of NEGFs for QCL simulation is discussed in [25]. This NEGFs code is paralellized [3] and it can simultaneously run in as many threads as available in the CPU (12 for Mass181 and Mass182, and 8 for Myon and Gluon). In contrast, LQCL is not paralellized and uses a single thread for the calculations. To establish a comparison between both codes, the unparalellized version of the NEGFs code, running on a single thread, was used.

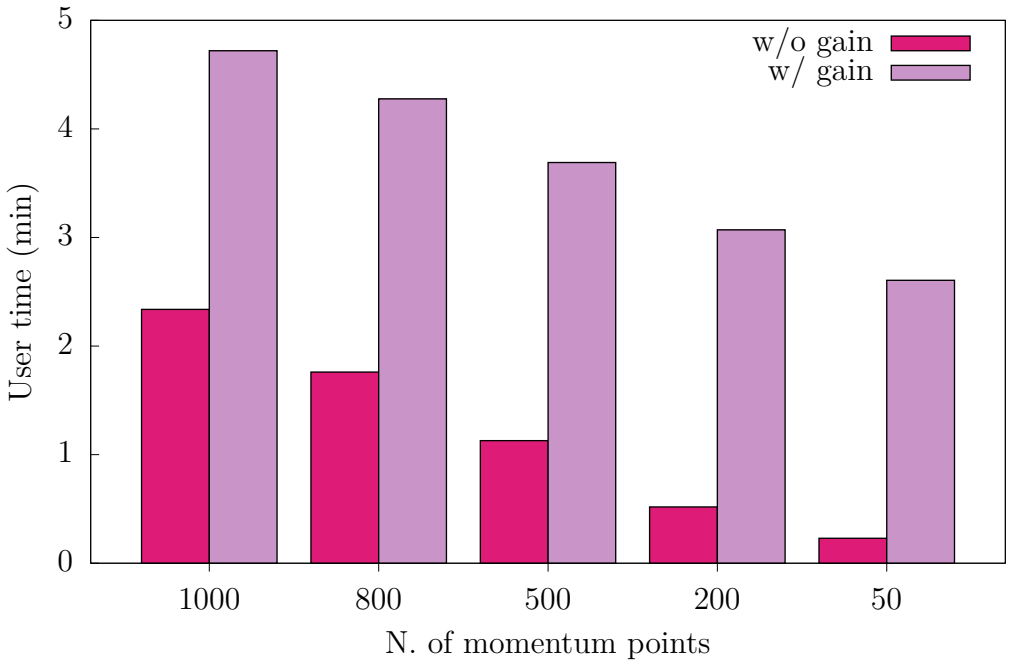

(a) LQCL simulation of QCL with 3 WS states [17].

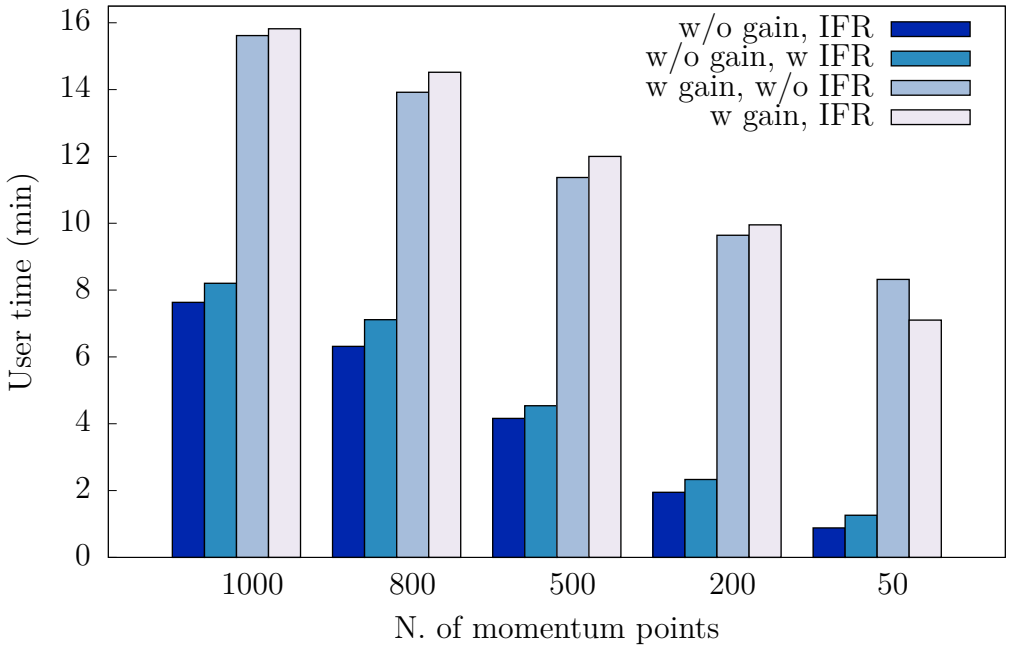

(b) LQCL simulation of QCL with 5 WS states [50].

Figure 5.4: User time as a function of the number of points for longitudinal and transverse momenta. Simulations were done with (w) and without (w/o) computing 11 gain points (constructing a spectrum) and with or without IFR scattering.

Table 5.1: Comparison of the user time required to compute one I-V data point with the group's implementation of NEGFs [25] and the LQCL package for five THz-QCLs [16, 17, 22, 50, 38]. A single thread was used for both NEGFs and LQCL.

Device	N. of WS states	NEGFs (s)	LQCL (s)
Han *et al.* [17]	3	491.1	83.5
Fathololoumi *et al.* [16]	4	726.4	285.9
Li *et al.* [50]	5	1271.0	459.9
Dupont *et al.* [22]	5	1548.4	448.5
Williams *et al.* [38]	6	3069.6	629.9

Table 5.2: Comparison between the NEGFs code and LQCL of the user time required to compute gain. Using our group's implementation of NEGFs we compute a *single* data point at the design bias of the device; with LQCL, we compute a gain spectrum of 11 points. The devices shown are [16, 17, 22]. A single thread was used for both NEGFs and LQCL.

Device	N. of WS states	NEGFs (s)	LQCL (s)
Han *et al.* [17]	3	727.5	94.9
Fathololoumi *et al.* [16]	4	3261.0	470.5
Dupont *et al.* [22]	5	10447.1	688.7

The results of the comparison are shown in Table 5.1 and Table 5.2. In Table 5.1, we show the computation time for a single I-V data point using the NEGFs code and the LQCL package. The user time for NEGFs is reduced between 60% and 70% with the LQCL package. Nevertheless, LQCL's (and PERLind's) main advantage is that it allows us to obtain fast time-resolved results, i.e. gain. As we have discussed above, in LQCL gain spectrum can almost straightforwardly be obtained once the I-V curve is computed. In Table 5.2, we compare both methods for gain simulation. The time shown for NEGFs corresponds to a *single* gain point, while the time shown for LQCL is for a *complete gain spectrum* (11 data points). It is here where we see LQCL's power: the computation time is reduced between 85% and 90% when we compute gain with LQCL. Most importantly, it is fundamental to realize that LQCL provides a full spectrum at the design bias of the device while NEGFs require long times for a single data point.

Chapter 6 | Conclusion and Outlook

In this thesis, we have tested and analysed the scope and performance of the LQCL Python package. LQCL simulated quantum transport in QCLs based on a phenomenological and heuristic density matrix approach called PERLind [26]. Using LQCL, we have simulated eleven devices (eight THz-QCLs and three IR-QCLs) and compared LQCL's results to experimental data as well as our group's NEGFs code for QCL simulation [25].

We have found that the LQCL simulation package provides good qualitative results. The package manages to correctly reproduce the general trend of the current density as a function of the applied bias. In our simulations, we are able to observe parasitic currents, tunneling resonances and NDR regions where they have been experimentally reported for their respective devices. Moreover, the computed emission spectra peak at the experimental frequencies. Since the energy of the photoemissions entirely depends on the space between the levels, a correct gain spectrum asserts the validity of the theoretical approach we have used to compute the WS eigenbasis. It also supports the reliability of the Fortran package employed for the same purpose.

We have observed unexpected jumps and peaks in the I-V curves and discussed their origin. The energy levels in the QCL heterostructure are extended, and these aforementioned peaks arise when two levels are in resonance. To avoid such jumps and obtain a smoother I-V curve, we have found that the simulations need to be extended to more neighbours (second or third neighbours). Since the computation time increases accordingly, we have limited our simulations to first neighbours, keeping in mind that the accuracy can always be increased at those bias points where the peaks arise in a subsequent step. We have also discussed that the LQCL package does not provide satisfactory quantitative results: the current density is generally underestimated at high applied bias, and experimental maximum and threshold current density values are not reached. We have seen that extending the simulations to second and third neighbours yields a small increase in the current density, but it is not sufficient to reach experimental data. We have observed unphysical negative currents that arise from PERLind.

To understand the cause of the current density underestimation, we have studied the impact of temperature in the simulations. While at low applied bias it is correct to estimate $T_E \approx T_L$, such approximation becomes too crude at high applied bias, where heating effects become relevant. We have shown that there exists a correlation between the carrier excess temperature and the power to be dissipated per particle. In order to model temperature more accurately, we have proposed an energy balance equation to compute T_E at each bias point, similar to that in [31]. The results obtained show little improvement when compared to the simulations with a single, constant T_E. Nevertheless, the energy balance equation helps us see that LQCL's current underestimation greatly stems from its simplified treatment of temperatures. We argue that the lack of in-plane resolution limits LQCL's approach to temperature modeling. We are forced to assume that all QCL subbands are thermalized and share the same temperature. We have also included IFR scattering in the LQCL package, which has improved the results quantitatively.

We have compared LQCL's computation time with our group's implementation of NEGFs for QCL simulation. Such comparison shows LQCL is a fast and light simulation package; it is able to perform time-resolved computations, i.e. provide gain spectra, eight times faster than NEGFs. Nevertheless, the LQCL package allows further improvements. The computation time per data point can be reduced through parallelization. Currently, the Lindblad dissipators for LO-phonon, impurity and IFR scattering are constructed in series. As impurity scattering is associated to the largest number of numerical integrals, it bottlenecks the simulations; IFR scattering, on the other hand, is faster to compute as there is no overlap integral to be computed. The LQCL code could be parallelized by sending the subroutines that construct the dissipators for each scattering mechanism to different threads. Such parallelization could make room (and time) for the implementation of additional scattering mechanisms like alloy scattering, not discussed in this thesis due to its less important role in QCL transport.

Currently, LQCL's main limitation is its implementation of the subband electronic temperature. It is clear that a more accurate treatment of temperature requires assigning individual T_E to each subband. As an outlook for the project, it would be interesting to implement multi-subband energy balance equations as those in [63] in the package, instead of a single averaged T_E for all subbands. Then, it would possible to test whether the subband electronic temperatures have the large impact in the current density flow we have hypothesized in this thesis.

Overall, the LQCL package proves to be a useful and reliable tool for a first, fast approach to the active region of a QCL. Such initial approach could be later followed by more detailed and tailored simulations either including more periods and neighbours in the calculations or using robust methods like NEGFs [25]. LQCL's speed and lightness, specially for time-resolved computations of gain spectra, make it an ideal candidate to search for efficient QCLs via optimization algorithms. Indeed, the future of QCL simulations lies in aiding the experimental development of these devices by guiding researchers towards more efficient designs.

Fast simulation packages like LQCL enable a systematic search in the QCL parameter space (e.g. number of wells, alloy fraction or doping density). Optimized structures can yield higher operation temperatures and output powers. This is the idea behind the recently developed AFTERSHOQ (A Flexible Tool for Electromagnetic Radiation-emitting Semiconductor Heterostructure Optimization using Quantum models) [64]. Aftershoq is an interface for QCL simulations. It contains QCL parameters and material information, and creates a blueprint of the QCL structure. Then, it bridges it with the user's simulation code - in our case, LQCL - and can initiate a QCL optimization search using *Hilbert curves* [64]. The main condition for the appropriate use of this computational tool is to have a solid and reliable QCL simulation package which is, above all, fast. The results presented in this thesis indicate that LQCL is on the right track to become a strong candidate for future QCL simulations and device optimization.

Appendix

Chapter A | LO scattering

In this appendix, we will compute the LO-phonon scattering rate and construct the corresponding Lindblad dissipator following the scheme proposed by the PERLind approach in Chapter 3 of the thesis.

The LO-phonon scattering rate

The rate at which an electron transitions from an initial state $|i\rangle$ to a final state $|f\rangle$ emitting or absorbing a phonon is given by Fermi's Golden rule [30],

$$\Gamma_{i\to f} = \frac{2\pi}{\hbar} |\langle f| \hat{H}_{\text{el-ph}} |i\rangle|^2. \tag{A.1}$$

The Fhrölich hamiltonian, $H_{\text{el-ph}}$, given in eq. (2.1), accounts for the electron-phonon interaction. This interaction involves a momentum exchange: the electron jumps from an initial state with momentum $\boldsymbol{k}$ to a final state with momentum $\boldsymbol{k'}$ such that a phonon with momentum $\boldsymbol{q} = \boldsymbol{k'} - \boldsymbol{k}$ is emitted or absorbed. In the second quantization formalism, the initial and final states for the absorption of a phonon can be represented as [30]

$$|i\rangle = \left| n^e_{\boldsymbol{k}+\boldsymbol{q}}, n^e_{\boldsymbol{k}}; n^{ph}_{\boldsymbol{q}} \right\rangle, \tag{A.2}$$

$$|f\rangle = \left| n^e_{\boldsymbol{k}+\boldsymbol{q}} + 1, n^e_{\boldsymbol{k}} - 1; n^{ph}_{\boldsymbol{q}} - 1 \right\rangle, \tag{A.3}$$

where n^e and n^{ph} indicate the number of electrons and phonons in a given state, respectively. Substituting these states in equation (A.1), the scattering rate is given by [26, 30]

$$\Gamma_{\alpha,\boldsymbol{k}\to\beta,\boldsymbol{k}+\boldsymbol{q}} = \frac{2\pi}{\hbar} \sum_{q_z} |M^{q_z}_{\beta\alpha}|^2 \Big[|\mathrm{g}_{-\boldsymbol{q},-q_z}|^2 \delta(E_{\beta,\boldsymbol{k}+\boldsymbol{q}} - E_{\alpha,\boldsymbol{k}} + \hbar\omega_{LO})[f_B(\hbar\omega_{LO}) + 1] + |\mathrm{g}_{\boldsymbol{q},q_z}|^2 \delta(E_{\beta,\boldsymbol{k}+\boldsymbol{q}} - E_{\alpha,\boldsymbol{k}} + \hbar\omega_{LO}) f_B(\hbar\omega_{LO}) \Big], \tag{A.4}$$

where $f_B(E)$ is the Bose-Einstein boson distribution for phonons, $M^{q_z}_{\beta\alpha}$ is the overlap integral in (2.2) and $E_{\alpha,\boldsymbol{k}} = E_\alpha + \frac{\hbar|\boldsymbol{k}|^2}{2m}$, where E_α is the energy of the α quantized level. The total rate is obtained by averaging over the lateral electronic degrees of freedom [26],

$$R_{\alpha\to\beta} = \frac{\sum_{\boldsymbol{k},\boldsymbol{k}+\boldsymbol{q}} f_{\alpha,\boldsymbol{k}}\, \Gamma_{\alpha,\boldsymbol{k}\to\beta,\boldsymbol{k}+\boldsymbol{q}}}{\sum_{\boldsymbol{k}} f_{\alpha,\boldsymbol{k}}}. \tag{A.5}$$

Electrons are assumed to occupy thermal distributions in the in-plane direction, $f_{\alpha,\boldsymbol{k}} \propto e^{-E_{\boldsymbol{k}}/k_BT}$. The denominator in (A.5) is then given by

$$\sum_{\boldsymbol{k}} f_{\alpha,\boldsymbol{k}} = \frac{A}{(2\pi)^2} \int_0^{2\pi} d\phi \int_0^\infty k\, dk\, e^{-E_k/k_BT} = \frac{A}{(2\pi)} \frac{m}{\hbar^2} k_BT. \tag{A.6}$$

To sum over all lateral degrees of freedom in the numerator of (A.5), the delta function in (A.4), which accounts for energy conservation, must be rewritten. We notice that

$$E_{\beta,\boldsymbol{k}+\boldsymbol{q}} - E_{\alpha,\boldsymbol{k}} \pm \hbar\omega_{LO} = E_\beta - E_\alpha + \frac{\hbar^2|\boldsymbol{k}+\boldsymbol{q}|^2}{2m} - \frac{\hbar^2 k^2}{2m} \pm \hbar\omega_{LO} = \\ \Delta_{\alpha\beta} + \frac{\hbar^2 q^2}{2m} + \frac{\hbar^2}{m} kq\cos\phi \pm \hbar\omega_{LO} = \Delta_{\alpha\beta,\boldsymbol{q}} + \frac{\hbar^2}{m} kq\cos\phi \pm \hbar\omega_{LO}. \quad \text{(A.7)}$$

Using the identity

$$\delta(f(k)) = \sum_i \frac{\delta(k-k_i)}{|f'(k_i)|}, \quad \text{(A.8)}$$

where k_i is the i-th root of the function $f(k)$, the delta function is expressed as

$$\delta(E_{\beta,\boldsymbol{k}+\boldsymbol{q}} - E_{\alpha,\boldsymbol{k}} \pm \hbar\omega_{LO}) = \frac{m}{\hbar^2}\frac{\sec\phi}{q}\delta\left(k + \frac{m}{\hbar^2}\frac{\sec\phi}{q}(\Delta_{\alpha\beta,\boldsymbol{q}} \pm \hbar\omega_{LO})\right). \quad \text{(A.9)}$$

The integral [26]

$$\int_0^{2\pi} \sec^2\phi e^{-a\sec^2\phi} = 2e^{-a}\sqrt{\frac{\pi}{a}} \quad \text{(A.10)}$$

allows us to compute the denominator in (A.5) (for the emission of a LO phonon):

$$\sum_{\boldsymbol{k},\boldsymbol{k}+\boldsymbol{q}} f_{\alpha,\boldsymbol{k}}\Gamma_{\alpha,\boldsymbol{k}\to\beta,\boldsymbol{k}+\boldsymbol{q}} = C_- \sum_{\boldsymbol{k}+\boldsymbol{q}} \int \frac{dq_z}{(2\pi)}\frac{|M^{q_z}_{\beta\alpha}|^2}{q^2+q_z^2}\frac{A}{(2\pi)^2}\times \\ \times \int_0^{2\pi} d\phi \int_0^\infty k\, dk e^{-E_k/k_BT}\frac{m}{\hbar^2}\frac{\sec\phi}{q}\delta\left(k + \frac{m}{\hbar^2}\frac{\sec\phi}{q}(\Delta_{\alpha\beta,\boldsymbol{q}} \pm \hbar\omega_{LO})\right), \quad \text{(A.11)}$$

where C_- is a constant corresponding to the emission of a phonon. Finally, the total scattering rate for emission is given by

$$R^{\text{em.}}_{\alpha\to\beta} = \tilde{C}_- \int \frac{\mathrm{d}q_z}{2\pi}\int_0^\infty \frac{\mathrm{d}q}{2\pi}\frac{\exp\left[-\frac{(\Delta_{\alpha\beta,\boldsymbol{q}}+\hbar\omega_{LO})^2}{4E_{\boldsymbol{q}}k_BT}\right]}{q^2+q_z^2}|M^{q_z}_{\beta\alpha}|^2, \quad \text{(A.12)}$$

where $\tilde{C}_-$ is

$$\tilde{C}_- = -f_B(\hbar\omega_{LO})\frac{2\pi}{\hbar}\frac{e^2\hbar\omega_{LO}}{2\epsilon_0\epsilon_p}\sqrt{\frac{m_c}{2\pi\hbar^2 k_B T}} \quad \text{(A.13)}$$

The scattering rate for absorption is computed in an identical way, with some sign changes. The derivation above has followed those in [26] and [30]. The interested reader is referred there for further details on the calculation of the rates.

Construction of the Lindblad dissipator

To build a matrix element for the LO-phonon Lindblad dissipator (3.7), it is sufficient to identify the terms that give spatial and energy resolution from (A.12). The integral $M^{q_z}_{\beta\alpha}$ in eq. (2.2) contains the overlap of eigenstates α and β as a result of the electron-phonon perturbation potential. The remaining factors in eq. (A.12) modulate the intensity of the interaction and contain energy information. Therefore, the *building blocks* for the Lindblad coupling tensor in equation (3.4) associated to the emission of a LO-phonon, are given by

$$L^{j\ (\text{LO})}_{\alpha\beta} = M^{q_z}_{\alpha\beta}, \quad \text{(A.14)}$$

$$f_{q_z}^{(\mathrm{LO})}(E_\beta - E_\alpha) = \tilde{C}_- \int_0^\infty \frac{\mathrm{d}q}{2\pi} \frac{\exp\left[-\frac{(\Delta_{\alpha\beta,\vec{q}}+\hbar\omega_{LO})^2}{4E_{\boldsymbol{q}}k_BT}\right]}{q^2+q_z^2}. \tag{A.15}$$

(A.14) and (A.15) are combined to form the matrix element (3.7), which eventually yields (3.9) after summing over all q_z.

Chapter B | Impurity scattering

In this appendix, we are interested in computing the impurity scattering rate to build the corresponding Lindblad dissipator within the PERLind approach. As introduced in subsection 2.1.2, the screened Coulombian potential that accounts for the interaction of an electron with an ionic impurity at position z_i and charge Z_i is

$$V_{\text{Coulomb}} = \frac{e^2 Z_i}{4\pi\epsilon_0\epsilon_r} \frac{e^{-\lambda\sqrt{|\boldsymbol{r}-\boldsymbol{r}_i|^2+(z-z_i)^2}}}{\sqrt{|\boldsymbol{r}-\boldsymbol{r}_i|^2+(z-z_i)^2}}. \tag{B.1}$$

Here, $\boldsymbol{r}$ is a two-dimensional vector $\boldsymbol{r} = (x, y)$ and λ is the screening length.

Fourier transform of the screened Coulomb potential

In order to simplify the calculations, we compute the Fourier transform of potential (B.1). For convenience and only for this subsection, $\boldsymbol{q}$ and $\boldsymbol{r}$ will now refer to 3-dimensional vectors. The Fourier transform of the potential for an impurity i is given by an expansion in a plane wave basis

$$V_{\text{Coulomb}} = \frac{1}{V}\sum_{\boldsymbol{q}} V_{\boldsymbol{q}}^{\lambda} e^{i\boldsymbol{q}\cdot(\boldsymbol{r}-\boldsymbol{r}_i)}. \tag{B.2}$$

The coefficient $V_{\boldsymbol{q}}^{\lambda}$ can be computed by multiplying both sides of equation (B.2) by $\int d^3r\, e^{-i\boldsymbol{q'}\cdot\vec{r}}$, applying the orthogonality properties of plane waves and taking the continuous limit $\frac{1}{V}\sum_{\boldsymbol{q}} \to \frac{1}{(2\pi)^3}\int d^3q$,

$$V_{\boldsymbol{q}}^{\lambda} = \int d^3r\, \frac{e^2 Z_i}{4\pi\epsilon_0\epsilon_r} \frac{e^{-\lambda r}}{r} e^{-i\boldsymbol{q'}\cdot\boldsymbol{r}}, \tag{B.3}$$

with $r = \sqrt{|\boldsymbol{r}-\boldsymbol{r}_i|^2+(z-z_i)^2}$. We write the integral in spherical coordinates,

$$V_{\boldsymbol{q}}^{\lambda} = \frac{e^2 Z_i}{4\pi\epsilon_0\epsilon_r} \int_0^{2\pi} d\phi \int_0^{\pi} \sin\theta d\theta \int_0^{\infty} r\, e^{-\lambda r} e^{-i|\boldsymbol{q}|\,|\boldsymbol{r}|\cos\theta} dr. \tag{B.4}$$

The integral in ϕ can immediately be solved and the one in θ is easily performed by changing $\cos\theta = u$, which finally yields

$$V_{\boldsymbol{q}}^{\lambda} = \frac{e^2 Z_i}{\epsilon_0\epsilon_r} \int_0^{\infty} \frac{e^{-\lambda r}}{q} \sin(qr) dr = \frac{e^2 Z_i}{\epsilon_0\epsilon_r} \frac{1}{q} \operatorname{Im}\left[\int_0^{\infty} e^{(iq-\lambda)r}\right] = \frac{e^2 Z_i}{\epsilon_0\epsilon_r} \frac{1}{\lambda^2+q^2} \tag{B.5}$$

The scattering matrix element

The electron-impurity scattering element is given by

$$V_{\alpha,\boldsymbol{k}\to\beta,\boldsymbol{k'}} = \int d^2r \int dz\, \Psi^{\star}_{\alpha,\boldsymbol{k}}(\boldsymbol{r}, z) V_{\text{Coulomb}} \Psi_{\beta,\boldsymbol{k'}}(\boldsymbol{r}, z), \tag{B.6}$$

where the wavefunctions $\Psi_{\alpha,\boldsymbol{k}}$ are those in eq. (2.9). For a single impurity at z_i, we introduce the Fourier expansion in (B.2) into (B.6)

$$V^i_{\alpha,\boldsymbol{k}\to\beta,\boldsymbol{k'}} = \frac{1}{A^2L}\sum_{\boldsymbol{q}}\sum_{q_z}\frac{e^2Z_i}{\epsilon_0\epsilon_r}\int d^2r\int dz\,\psi^\star_{\alpha,\boldsymbol{k}}\,e^{i\,q_z(z-z_i)}\,\psi_{\beta,\boldsymbol{k'}}\frac{e^{i(\boldsymbol{q}+\boldsymbol{k'}-\boldsymbol{k})\cdot\boldsymbol{r}}}{q^2+q_z+\lambda^2}e^{-i\boldsymbol{q}\cdot\boldsymbol{r}_i}. \tag{B.7}$$

The expression above can be simplified as follows. First, we use the integral

$$\int d^2r\,e^{i(\boldsymbol{q}+\boldsymbol{k'}-\boldsymbol{k})\cdot\boldsymbol{r}} = (2\pi)^2\delta(\boldsymbol{q}+\boldsymbol{k'}-\boldsymbol{k}), \tag{B.8}$$

which allows us to eliminate the sum in $\boldsymbol{q}$ together with the $(2\pi)^2$ and one 1/A factor in (B.7). The Dirac delta establishes the momentum conservation during the scattering process, where $\boldsymbol{q}=\boldsymbol{k}-\boldsymbol{k'}$. The integral in q_z can be solved in the complex plane, applying the Residue theorem,

$$\frac{1}{L}\sum_{q_z}\frac{e^{i\,q_z(z-z_i)}}{q^2+q_z+\lambda^2} = \frac{1}{4\pi}\int_0^\infty dq_z\,\frac{e^{i\,q_z(z-z_i)}}{q^2+q_z+\lambda^2} = 2\pi i\sum_m \mathrm{Res}\left(\frac{e^{i\,q_z^m(z-z_i)}}{q^2+q_z^m+\lambda^2}\right). \tag{B.9}$$

The poles of the function are located in

$$q_z^\pm = \pm i\sqrt{q^2+\lambda^2}. \tag{B.10}$$

We choose the q_z^+ pole, which is located north of the $\mathrm{Re}(q_z)$ axis, as we need to ensure that the corresponding line integral arising in the complex plane vanishes. We then get

$$\frac{1}{4\pi}\int_0^\infty dq_z\,\frac{e^{i\,q_z(z-z_i)}}{q^2+q_z+\lambda^2} = \frac{1}{2}\frac{e^{-\sqrt{q^2+\lambda^2}|z-z_i|}}{\sqrt{q^2+\lambda^2}}. \tag{B.11}$$

Finally, the resulting scattering matrix element can be written as

$$V^i_{\alpha,\boldsymbol{k}\to\beta,\boldsymbol{k}+\boldsymbol{q}} = \frac{e^2Z_i}{2\epsilon_0\epsilon_r A}\frac{e^{-i\boldsymbol{q}\cdot r_i}}{\sqrt{q^2+\lambda^2}}M^{i,q}_{\alpha,\beta}, \tag{B.12}$$

where

$$M^{i,q}_{\alpha,\beta} = \int dz\,\psi^\star_\alpha(z)\psi_\beta(z)e^{-\sqrt{q^2+\lambda^2}|z-z_i|}. \tag{B.13}$$

The impurity scattering rate

The impurity scattering rate is given by Fermi's Golden Rule [26]

$$\Gamma_{\alpha,\boldsymbol{k}\to\beta,\boldsymbol{k}+\boldsymbol{q}} = \frac{2\pi}{\hbar}|\langle U_{\alpha,\boldsymbol{k}\to\beta,\boldsymbol{k}+\boldsymbol{q}}\rangle|^2\delta(E_{\beta,\boldsymbol{k}+\boldsymbol{q}}-E_{\alpha,\boldsymbol{k}}). \tag{B.14}$$

Here, the squared matrix element must be summed over all impurities i. In order to do so, we will assume an averaged distribution of the impurities in the period [26],

$$|\langle U_{\alpha,\boldsymbol{k}\to\beta,\boldsymbol{k}+\boldsymbol{q}}\rangle|^2 = AN_{2\mathrm{D}}\sum_i w_i|V^i_{\alpha,\boldsymbol{k}\to\beta,\boldsymbol{k}+\boldsymbol{q}}|^2, \tag{B.15}$$

where w_i weights the distribution of impurities and $N_{2\mathrm{D}}$ is the period impurity density. Just as we did to compute the total LO-scattering rate, we need to sum over all the in-plane degrees of freedom according to eq. (A.5). Once again, we assume an in-plane thermal distribution for the electrons. Performing the integral in $\boldsymbol{k}$ as we did in Appendix A and using the normalization eq. (A.6), we are left with the following total rate

$$R_{\alpha\to\beta} = \sum_i\sum_{\boldsymbol{q}}\frac{2\pi}{\hbar}w_iN_{2\mathrm{D}}\left(\frac{e^2Z_i}{2\epsilon_0\epsilon_r}\right)^2\sqrt{\frac{m_c}{2\pi\hbar^2k_BT}}\frac{e^{-\Delta_{\alpha\beta,\boldsymbol{q}}/4E_{\boldsymbol{q}}K_BT}}{q^2+\lambda^2}\,|M^{i,q}_{\beta\alpha}|^2 \tag{B.16}$$

Construction of the Lindblad dissipator

The information about the locality of the transition is contained within the overlap integral (B.13), which includes the quantized wells levels as well as information about the scattering potential for a single impurity. Therefore, according to the PERLind approach, we associate a jump operator to it,

$$L_{\alpha\beta}^{i,q\ (\mathrm{imp})} = M_{\alpha\beta}^{i,q}. \tag{B.17}$$

It is important here to notice that we will have as many jump operators as impurities. The energy-dependent function that modulates the strength of the transition can be, as we did for LO-scattering, inferred from the scattering rate (B.16),

$$f_{i,q}^{(\mathrm{imp})}(E_\beta - E_\alpha) = \frac{2\pi}{\hbar} w_i N_{2\mathrm{D}} \left(\frac{e^2}{2\epsilon_0\epsilon_s}\right)^2 \sqrt{\frac{m_c}{2\pi\hbar k_B T}}\, \frac{e^{-\frac{(\Delta_{\alpha\beta,\boldsymbol{q}})^2}{4E_{\boldsymbol{q}}k_B T}}}{q^2+\lambda^2}. \tag{B.18}$$

Using (B.17) and (B.18), we construct the matrix element for the Lindblad dissipator (3.7) that accounts for impurity scattering.

Chapter C | IFR scattering

In this appendix, we construct the Lindblad dissipator for IFR scattering within the PERLind approach. For that purpose, we will first compute the total IFR scattering rate, and identify the energy and space-resolving elements required by the approach in a subsequent step.

The IFR scattering rate

IFR scattering is an elastic scattering that originates from the random fluctuations of barrier width at the interfaces of a semiconductor heterostructure (see Fig. 2.3). Such fluctuations can be modelled by a potential [10]

$$V = \pm V_0 \left[\theta(z - z_0) - \theta(z - z_0 - \Delta(\boldsymbol{r}))\right], \tag{C.1}$$

where V_0 is the band offset, z_0 is the average interface position and $\Delta(\boldsymbol{r})$ is the variation in height. The function $\theta(z - z_0)$ is known as the *Heaviside* function, defined as

$$\theta(z - z_0) = \begin{cases} 0 & z < z_0 \\ 1 & z \geq z_0 \end{cases}$$

The potential matrix element, accounting for a single interface at z_0, is given by [10]:

$$V_{\alpha,\boldsymbol{k}\to\beta,\boldsymbol{k}+\boldsymbol{q}} = \pm\frac{V_0}{A}|\psi_\alpha(z_0)\psi^\star_\beta(z_0)| \int \mathrm{d}^2 r\ \Delta(\boldsymbol{r}) e^{i\,\boldsymbol{q}\cdot\boldsymbol{r}} \tag{C.2}$$

where the eigenfunctions have been approximated to

$$\psi_{\alpha,\beta}(z_n + \Delta(\boldsymbol{r})) \approx \psi_{\alpha,\beta}(z_n). \tag{C.3}$$

This approximation is reasonable because height fluctuations are assumed to be small (0.1-0.4 nm) [34]. The squared matrix element is given by

$$|V_{\alpha,\boldsymbol{k}\to\beta,\boldsymbol{k}+\boldsymbol{q}}|^2 = \frac{V_0^2}{A^2}|\psi_\alpha(z_0)\psi^\star_\beta(z_0)|^2 \int \mathrm{d}^2 d \left[e^{i\boldsymbol{q}\cdot\boldsymbol{d}} \int \mathrm{d}^2 r \Delta(\boldsymbol{r})\Delta(\boldsymbol{r}+\boldsymbol{d})\right] \tag{C.4}$$

where

$$F(\boldsymbol{q}) = \int \mathrm{d}^2 d\ e^{i\boldsymbol{q}\cdot\boldsymbol{d}} \int \mathrm{d}^2 r \Delta(\boldsymbol{r})\Delta(\boldsymbol{r}+\boldsymbol{d}) \tag{C.5}$$

corresponds to the Fourier transform, $F(\boldsymbol{q})$, of the fluctuation correlation function,

$$\langle \Delta(\boldsymbol{r})\Delta(\boldsymbol{r}+\boldsymbol{d})\rangle = \int \mathrm{d}^2 r \Delta(\boldsymbol{r})\Delta(\boldsymbol{r}+\boldsymbol{d}). \tag{C.6}$$

As discussed in section 2.1, the correlation function can be modelled as a Gaussian (2.6) or an Exponential function (2.7) [3, 10]. The corresponding Fourier transforms are

$$F(\boldsymbol{q}) = \pi\Delta^2\Lambda^2 \exp\left(-\frac{\Lambda^2|\boldsymbol{q}|^2}{4}\right) \tag{C.7}$$

for a Gaussian correlation function and

$$F(\boldsymbol{q}) = \frac{2\pi\tilde{\Delta}^2\tilde{\Lambda}^2}{\left(1+\tilde{\Delta}^2|\boldsymbol{q}|^2\right)^{3/2}} \tag{C.8}$$

for exponential modeling. To compute the scattering rate, we turn to Fermi's Golden Rule and include the contribution of all interfaces at positions z_i,

$$\Gamma_{\alpha,\boldsymbol{k}\to\beta,\boldsymbol{k}+\boldsymbol{q}} = \frac{2\pi}{\hbar}\frac{V_0^2}{A^2}\sum_i |\psi_\alpha(z_i)\psi_\beta^\star(z_i)|^2 |F(\boldsymbol{q})|^2 \delta(E_{\beta,\boldsymbol{k}+\boldsymbol{q}} - E_{\alpha,\boldsymbol{k}}). \tag{C.9}$$

As discussed in Appendix A, the total rate is obtained by averaging over the in-plane degrees of freedom as given by eq. (A.5). The normalization constant can be found in (A.6). We can perform the integral in $\boldsymbol{k}$,

$$\frac{A}{(2\pi)^2}\int \mathrm{d}\phi \int k\,\mathrm{d}k\,\delta(E_{\beta,\boldsymbol{k}+\boldsymbol{q}} - E_{\alpha,\boldsymbol{k}}) = \frac{A}{2\pi\hbar}\sqrt{\frac{m}{2\pi k_B T}} e^{\left[-\frac{(\Delta_{\alpha\beta,\boldsymbol{q}})^2}{4E_{\boldsymbol{q}}k_B T}\right]}, \tag{C.10}$$

where the identity (A.8) and integral (A.10) have been used. The averaged rate is

$$R_{\alpha\to\beta} = \sum_{\boldsymbol{q}}\sum_i \frac{V_0^2}{A\hbar^2}\sqrt{\frac{m}{2\pi k_B T}}\,|\psi_\alpha(z_i)\psi_\beta^\star(z_i)|^2\,|F(\boldsymbol{q})|^2\,e^{\left[-\frac{(\Delta_{\alpha\beta,\boldsymbol{q}})^2}{4E_{\boldsymbol{q}}k_B T}\right]}. \tag{C.11}$$

Construction of the Lindblad dissipator

The jump operators to construct the Lindblad dissipator are derived from the averaged rate (C.11). The identification of the operators can be done in two different ways: either we consider the interfaces to be correlated and hence, work with a single operator or assign an operator to each interface. Since the latter scenario is much more likely, we assign an operator to each interface i,

$$L^i_{\alpha\beta} = |\psi_\alpha(z_i)\psi_\beta^\star(z_i)|. \tag{C.12}$$

This function includes information about the spatial overlap of the eigenfunctions as a result of the scattering potential. The function that accounts for the energy dependence is given by

$$f(E_\beta - E_\beta) = \frac{V_0^2}{A\hbar^2}\sqrt{\frac{m}{2\pi k_B T}}|F(\boldsymbol{q})|^2\,e^{\left[-\frac{(\Delta_{\alpha\beta,\boldsymbol{q}})^2}{4E_{\boldsymbol{q}}k_B T}\right]}, \tag{C.13}$$

from where we can get $\tilde{L}^i_{ab} = \sqrt{f(E_b - E_a)}L^i_{ab}$. The coupling tensor is constructed by adding the contributions of every interface i and integrating over $\boldsymbol{q}$.

Bibliography

[1] *Press release*, European Physical Society (2014), accessed: 2019-04-02

[2] 2015 International Year of Light and Light-Based Technologies, accessed: 2019-04-02

[3] M. Franckié, *Modeling Quantum Cascade Lasers: The Challenge of Infra-Red Devices*, Ph.D. thesis, Lund University (2016)

[4] B. S. Williams, *Terahertz quantum-cascade lasers*, Nat. Photonics **1**, 517 (2007)

[5] B. Ferguson and X.-C. Zhang, *Materials for terahertz science and technology*, Nature Materials **1**, 26 (2002)

[6] J. Faist, F. Capasso, D. L. Sivco, C. Sirtori, A. L. Hutchinson, and A. Y. Cho, *Quantum cascade laser*, Science **264**, 553 (1994)

[7] L. Esaki and R. Tsu, *Superlattice and negative differential conductivity in semiconductors*, IBM J. Res. Dev. **14**, 61 (1970)

[8] O. Cathabard, R. Teissier, J. Devenson, J. C. Moreno, and A. N. Baranov, *Quantum cascade lasers emitting near 2.6 μm*, Appl. Phys. Lett. **96**, 141110 (2010)

[9] G. Scalari, D. Turcinková, J. Lloyd-Huges, M. I. Amanti, M. Fischer, M. Beck, and J. Faist, *Magnetically assited quantum cascade laser emitting from 740 ghz to 1.4 thz*, Applied Physics Letters **97**, 081110 (2010)

[10] C. Jirauschek and T. Kubis, *Modeling techniques for quantum cascade lasers*, Appl. Phys. Rev. **1**, 011307 (2014)

[11] R. F. Curl, F. Capasso, C. Gmachl, A. A. Kosterev, B. McManus, R. Lewicki, M. Pusharsky, G. Wysocki, and F. K. Tittel, *Quantum cascade lasers in chemical physics*, Chem. Phys. Lett. **487**, 1 (2010)

[12] J. Faist, *Quantum Cascade Lasers* (Oxford University Press, Oxford, 2013)

[13] G. P. Williams, *Filling the THz gap—high power sources and applications*, Reports on Progress in Physics **69**, 301 (2005)

[14] R. Köhler, A. Tredicucci, F. Beltram, H. E. Beere, E. H. Linfield, A. G. Davies, D. A. Ritchie, R. C. Iotti, and F. Rossi, *Terahertz semiconductor-heterostructure laser*, Nature **417**, 156 (2002)

[15] J. Faist, F. Capasso, C. Sirtori, D. L. Sivco, A. L. Hutchinson, and A. Y. Cho, *Room temperature mid-infrared quantum cascade lasers*, Electronics Letters **32**, 560 (1996)

[16] S. Fathololoumi, E. Dupont, C. Chan, Z. Wasilewski, S. Laframboise, D. Ban, A. Mátyás, C. Jirauschek, Q. Hu, and H. C. Liu, *Terahertz quantum cascade lasers operating up to $\sim$ 200 K with optimized oscillator strength and improved injection tunneling*, Opt. Express **20**, 3866 (2012)

[17] Y. J. Han, L. H. Li, A. Grier, L. Chen, A. Valavanis, J. Zhu, J. R. Freeman, N. Isac, R. Colombelli, P. Dean, A. G. Davies, and E. H. Linfield, *Extraction-controlled terahertz frequency quantum cascade lasers with a diagonal lo-phonon extraction and injection stage*, Optics Express **24**, 28583 (2016)

[18] D. Winge, *Quantitative Modeling of Gain in Quantum Cascade Lasers under Operational Intensities*, Ph.D. thesis, Lund University (2016)

[19] R. F. Kazarinov and R. A. Suris, *Possibility of the amplification of electromagnetic waves in a semiconductor with a superlattice*, Sov. Phys. Semicond. **5**, 707 (1971)

[20] Y. Yao, A. Hoffman, and C. F. Gmachl, *Mid-infrared quantum cascade lasers*, Nature Photonics **6**, 432 (2012)

[21] C. Gmachl, F. Capasso, D. L. Sivco, and A. Y. Cho, *Recent progress in quantum cascade lasers and applications*, Rep. Prog. Phys. **64**, 1533 (2001)

[22] E. Dupont, S. Fathololoumi, Z. R. Wasilewski, G. Aers, S. R. Laframboise, M. Lindskog, S. G. Razavipour, A. Wacker, D. Ban, and H. C. Liu, *A phonon scattering assisted injection and extraction based terahertz quantum cascade laser*, J. Appl. Phys. **111**, 073111 (2012)

[23] M. Franckié, L. Bosco, M. Beck, C. Bonzon, E. Mavrona, G. Scalari, A. Wacker, and J. Faist, *Two-well quantum cascade laser optimization by non-equilibrium Green's function modelling*, Appl. Phys. Lett. **112**, 021104 (2018)

[24] A. Wacker, *Transport in nanostructures: A comparison between nonequilibrium green functions and density matrices*, in *Advances in Solid State Phyics*, edited by B. Kramer, p. 199 (Springer, Berlin, 2001)

[25] A. Wacker, M. Lindskog, and D. O. Winge, *Nonequilibrium Green's function model for simulation of quantum cascade laser devices under operating conditions*, IEEE J. Sel. Top. Quant. **19**, 1200611 (2013)

[26] G. Kiršanskas, M. Franckié, and A. Wacker, *Phenomenological position and energy resolving Lindblad approach to quantum kinetics*, Phys. Rev. B **97**, 035432 (2018)

[27] B. A. Burnett, A. Pan, C. O. Chui, and B. S. Williams, *Robust density matrix simulation of terahertz quantum cascade lasers*, IEEE Trans. THz Sci. Techn. **8**, 492 (2018)

[28] A. Wacker, *Simulating quantum cascade lasers: The challenge to quantum theory*, inprint (2018)

[29] R. Ferreira and G. Bastard, *Evaluation of some scattering times for electrons in unbiased and biased single- and multiple-quantum-well structures*, Phys. Rev. B **40**, 1074 (1989)

[30] O. Madelung, *Introduction to Solid-State Theory* (Springer Berlin Heidelberg, Berlin, Heidelberg, 1978)

[31] P. Harrison, D. Indjin, and R. W. Kelsall, *Electron temperature and mechanisms of hot carrier generation in quantum cascade lasers*, Journal of Applied Physics **92**, 6921 (2002)

[32] R. C. Iotti and F. Rossi, *Microscopic theory of quantum-cascade lasers*, Semicond. Sci. Technol. **19**, S323 (2004)

[33] D. Vasileska, *Scattering mechanisms*, Lecture Notes at Network for Computational Nanotechnology, nanoHUB

[34] M. Franckié and D. O. Winge, *Impact of interface roughness distributions on the operation of quantum cascade lasers*, Opt. Express **23**, 5201 (2015)

[35] M. Franckié, D. O. Winge, J. Wolf, V. Liverini, E. Dupont, V. Trinité, J. Faist, and A. Wacker, *Impact of interface roughness distributions on the operation of quantum cascade lasers*, Optics Express **23**, 5201 (2015)

[36] G. Bastard, *Superlattice band structure in the envelope-function approximation*, Phys. Rev. B **24**, 5693 (1981)

[37] D. J. BenDaniel and C. B. Duke, *Space-charge effects on electron tunneling*, Phys. Rev. **152**, 683 (1966)

[38] B. S. Williams, S. Kumar, H. Callebaut, Q. Hu, and J. L. Reno, *Terahertz quantum-cascade laser operating up to 137 K*, Appl. Phys. Lett. **83**, 5142 (2003)

[39] A. Wacker, *Quantum cascade laser: An emerging technology*, in *Nonlinear Laser Dynamics*, edited by K. Lüdge (Wiley-VCH, Berlin, 2012)

[40] C. Weber, A. Wacker, and A. Knorr, *Density-matrix theory of the optical dynamics and transport in quantum cascade structures: The role of coherence*, Phys. Rev. B **79**, 165322 (2009)

[41] A. Wacker, *Coherence and spatial resolution of transport in quantum cascade lasers*, phys. stat. sol. (c) **5**, 215 (2008)

[42] R. K. Wangsness and F. Bloch, *The dynamical theory of nuclear induction*, Phys. Rev. **89**, 728 (1953)

[43] A. G. Redfield, *On the theory of relaxation processes*, IBM J. Res. Dev. **1**, 19 (1957)

[44] G. Lindblad, *On the generators of quantum dynamical semigroups*, Commun. Math. Phys. **48**, 119 (1976)

[45] V. Gorini, A. Kossakowski, and E. C. G. Sudarshan, *Completely positive dynamical semigroups of N-level systems*, J. Math. Phys. **17**, 821 (1976)

[46] B. Palmieri, D. Abramavicius, and S. Mukamel, *Lindblad equations for strongly coupled populations and coherences in photosynthetic complexes*, J. Chem. Phys. **130**, 204512 (2009)

[47] D. O. Winge, M. Franckié, and A. Wacker, *Simulating terahertz quantum cascade lasers: Trends from samples from different labs*, Journal of Applied Physics **120**, 114302 (2016)

[48] B. A. Burnett and B. S. Williams, *Density matrix model for polarons in a terahertz quantum dot cascade laser*, Phys. Rev. B **90**, 155309 (2014)

[49] L. Mahler, A. Tredicucci, R. Köhler, and F. Beltram, *High-performance operation of single-mode terahertz quantum cascade lasers with metallic gratings*, Applied Physics Letters **87**, 181101 (2005)

[50] L. Li, L. Chen, J. Zhu, J. Freeman, P. Dean, A. Valavanis, A. G. Davies, and E. H. Linfield, *Terahertz quantum cascade lasers with* > 1 *W output powers*, Electron. Lett. **50**, 309 (2014)

[51] S. Kumar, Q. Hu, and J. L. Reno, *186 K operation of terahertz quantum-cascade lasers based on a diagonal design*, Appl. Phys. Lett. **94**, 131105 (2009)

[52] A. Bismuto, R. Terazzi, M. Beck, and J. Faist, *Electrically tunable, high performance quantum cascade laser*, Appl. Phys. Lett. **96**, 141105 (2010)

[53] H. Page, C. Becker, A. Robertson, G. Glastre, V. Ortiz, and C. Sirtori, *300 K operation of a GaAs-based quantum-cascade laser at* $\lambda \approx 9\mu m$, Appl. Phys. Lett. **78**, 3529 (2001)

[54] H. Callebaut, S. Kumar, B. S. Williams, Q. Hu, and J. L. Reno, *Importance of electron-impurity scattering for electron transport in terahertz quantum-cascade lasers*, Appl. Phys. Lett. **84**, 645 (2004)

[55] T. Almqvist, D. O. Winge, E. Dupont, and A. Wacker, *Domain formation and self-sustained oscillations in quantum cascade lasers*, The European Physical Journal B **92**, 72 (2019)

[56] T. Almqvist, *Electric Field Domains in Quantum Cascade Lasers*, Master's thesis, Lunds University (2017)

[57] A. Albo and Y. V. Flores, *Carrier leakage dynamics in terahertz quantum cascade lasers*, IEEE Journal of Quantum Electronics **53** (2017)

[58] P. Harrison, *The nature of the electron distribution functions in quantum cascade lasers*, Appl. Phys. Lett. **75**, 2800 (1999)

[59] C. A. Evans, V. D. Jovanovic, D. Indjin, Z. Ikonic, and P. Harrison, *Investigation of thermal effects in quantum-cascade lasers*, IEEE Journal of Quantum Electronics **42**, 857 (2006)

[60] A. Z. Shi, Y.B. and I. Knezevic, *Self-consistent thermal simulation of gaas/algaas quantum cascade lasers*, J. Comput. Electron. **11**, 144 (2012)

[61] A. Albo and Q. Hu, *Investigating temperature degradation in thz quantum cascade lasers by examination of temperature dependence of output power*, Appl. Phys. Lett. **106**, 131108 (2015)

[62] A. Albo and Q. Hu, *Carrier leakage into the continuum in diagonal gaas/al0.15gaas terahertz quantum cascade lasers*, Appl. Phys. Lett. **107**, 241101 (2015)

[63] P. Slingerland, C. Baird, and R. H. Giles, *Application of multi-subband self-consistent energy balance method to terahertz quantum cascade lasers*, Semiconductor Science and Technology **27**, 065009 (2012)

[64] M. Franckié, *A flexible tool for em-radiation-emitting semiconductor heterostructure optimization using quantum models*, AFTERSHOQ, accessed: 2019-04-20